

AGN Feedback in Quiescent Galaxies at Cosmic Noon Traced by Ionized Gas Emission

LETIZIA BUGIANI,^{1,2} SIRIO BELLI,¹ MINJUNG PARK,³ REBECCA L. DAVIES,^{4,5} J. TREVOR MENDEL,^{5,6}
BENJAMIN D. JOHNSON,³ AMIR H. KHORAM,^{1,2} CHLOË BENTON,⁷ ANDREA CIMATTI,^{1,2} CHARLIE CONROY,³
RAZIEH EMAMI,³ JOEL LEJA,^{8,9,10} YIJIA LI,^{8,9} GABRIEL MAHESON,^{11,12} ELIJAH P. MATHEWS,^{8,9,10} ROHAN P. NAIDU,¹³
ERICA J. NELSON,⁷ SANDRO TACCHELLA,^{11,12} BRYAN A. TERRAZAS,¹⁴ AND RAINER WEINBERGER¹⁵

¹*Dipartimento di Fisica e Astronomia, Università di Bologna, Bologna, Italy.*

²*INAF, Osservatorio di Astrofisica e Scienza dello Spazio, Via Piero Gobetti 93/3, I-40129, Bologna, Italy.*

³*Center for Astrophysics — Harvard & Smithsonian, Cambridge, MA, USA.*

⁴*Centre for Astrophysics and Supercomputing, Swinburne University of Technology, Hawthorn, Victoria, Australia.*

⁵*ARC Centre of Excellence for All Sky Astrophysics in 3 Dimensions (ASTRO 3D), Australia.*

⁶*Research School of Astronomy and Astrophysics, Australian National University, Canberra, ACT, Australia.*

⁷*Department for Astrophysical and Planetary Science, University of Colorado, Boulder, CO, USA.*

⁸*Department of Astronomy & Astrophysics, The Pennsylvania State University, University Park, PA, USA.*

⁹*Institute for Gravitation and the Cosmos, The Pennsylvania State University, University Park, PA, USA.*

¹⁰*Institute for Computational & Data Sciences, The Pennsylvania State University, University Park, PA, USA.*

¹¹*Kavli Institute for Cosmology, University of Cambridge, Cambridge, UK.*

¹²*Cavendish Laboratory, University of Cambridge, Cambridge, UK.*

¹³*MIT Kavli Institute for Astrophysics and Space Research, Cambridge, MA, USA.*

¹⁴*Columbia Astrophysics Laboratory, Columbia University, New York, NY, USA.*

¹⁵*Leibniz Institute for Astrophysics, Potsdam, Germany.*

ABSTRACT

We analyze ionized gas emission lines in deep rest-frame optical spectra of 16 quiescent galaxies at redshift $1.7 < z < 3.5$ observed with JWST/NIRSpec by the Blue Jay survey. Robust detection of emission lines in 75% of the sample indicates the presence of ongoing ionizing sources in this passive population. The H α line luminosities confirm that the population is quiescent, with star formation rates that are at least ten times lower than the main sequence of star formation. The quiescent sample is clearly separate from the star-forming population in line diagnostic diagrams, and occupies a region usually populated by active galactic nuclei (AGN). Analysis of the observed line ratios, equivalent widths, and velocity dispersions leads us to conclude that in most cases the gas is ionized by AGN activity, despite the lack of X-ray detections. A subset of the sample also hosts ionized and/or neutral outflows. Our results show, for the first time using a representative sample, that low luminosity AGN are extremely common among quiescent galaxies at high redshift. These low luminosity AGN may play a key role in quenching star formation and in maintaining massive galaxies quiescent from Cosmic Noon to $z \sim 0$.

1. INTRODUCTION

At Cosmic Noon, the $z \sim 2$ peak of the cosmic star formation history (Madau & Dickinson 2014), most galaxies host a large amount of gas. However, this is also the epoch when the population of massive galaxies begins to transform into quiescent, gas-poor systems. The quenching of star formation is one of the key moments in a galaxy’s lifetime, but the physics behind it is still poorly understood, and requires more detailed studies of the first generation of quiescent galaxies.

Rest-frame optical emission lines due to ionized gas can provide a wealth of information about the physical conditions of high-redshift galaxies (Kewley et al. 2019,

and references therein). In star-forming galaxies, the ionization of the interstellar medium (ISM) is caused by young, massive stars; strong emission lines can also be produced by Active Galactic Nuclei (AGN), where the ionizing photon field is due to the actively feeding supermassive black hole (SMBH) in the center of the galaxy. Gas in the ISM can also be excited by shocks, which are more difficult to detect and can be caused by several different phenomena, including galactic-scale outflows, galaxy interactions, ram pressure stripping, and AGN-related activity such as jets and winds (Kewley et al. 2019). Mergers can also produce widespread shocks throughout galaxies which significantly affect the

emission-line spectrum (Medling et al. 2015), and stellar wind-induced shocks have been observed both in star-forming and starburst galaxies (Heckman et al. 2017; Ho et al. 2016).

Observations of ionized gas in high-redshift quiescent galaxies are necessary in order to constrain the physical conditions of these systems and to develop a comprehensive picture of galaxy quenching. However, the small amount of ionized gas left in these galaxies makes it challenging to detect and measure the emission lines, particularly at high redshift. Detections of very weak emission lines can be obtained more easily in the local universe. The presence of warm ionized gas in local quiescent galaxies, estimated to represent around 1% of their total ISM, has been known for a long time (Buson et al. 1993; Phillips et al. 1986): proposed explanations for the presence of this ionized phase have included external accretion of warm ISM from a companion galaxy (Bertola et al. 1992; Kim 1989), heat transfer from hot phase gas in the halo (Sparks et al. 1989; Voit & Donahue 1990), low-power nuclear activity (as in LINERs – Low-ionization nuclear emission-line regions); (Kim 1989; Shields 1992) and shocks (Heckman et al. 1989). The prevailing theory attributes the presence of warm gas to photoionization by hot evolved low-mass stars (HOLMES); (Binette et al. 1994; Macchetto et al. 1996). More recently, Cid Fernandes et al. (2011, 2010) used emission line ratios to distinguish so-called Emission Line Retired Galaxies (EL-RGs) with persistent ionized gas due to HOLMES photoionizing flux from true LINERs, i.e. galaxies that host a low-power AGN (see also Belfiore et al. 2016).

Beyond the limits of the local Universe the picture becomes much less clear, as the observations becomes more challenging; at $z > 1$ it is particularly difficult to detect faint emission lines from ionized gas because the rest-frame optical spectrum is observed at near-infrared wavelengths. Deep exposures with the largest ground-based telescopes have led to the detection of [NII] and H α emission lines in individual quiescent galaxies (Belli et al. 2017; Kriek et al. 2023) or in stacked spectra (Belli et al. 2019). The faintness of the observed emission lines rules out a substantial star formation rate in these galaxies; moreover, the [NII]/H α flux ratio is typically elevated and not consistent with ionization from young stars in HII regions. More detailed measurements of faint emission lines are possible in those rare $z \sim 2$ quiescent galaxies that are gravitationally lensed by a foreground cluster (Newman et al. 2015, 2018; Toft et al. 2017; Man et al. 2021). These studies confirm that young stars in HII regions contribute very little to both the ionization of the gas and the overall growth

of the galaxies (i.e., the measured specific star formation rates are very low). The ionization mechanism is often attributed to AGN feedback, but very little direct evidence for this exists given the scarcity of data; for example, the four emission lines required for the standard BPT diagram (Baldwin et al. 1981) have been measured in just two lensed galaxies (Newman et al. 2018).

Recently, the launch of JWST has begun a new era of sensitive near-infrared spectroscopy, free from contamination by atmospheric emission and absorption. Early JWST spectra of individual quiescent galaxies at $z > 2$ have revealed the presence of emission lines clearly due to AGN activity (Carnall et al. 2023; Belli et al. 2023; D’Eugenio et al. 2023), showcasing the potential of space-based spectroscopy for the study of faint emission from ionized gas at high redshift. In this work, we present the first comprehensive study of rest-frame optical emission lines in a representative sample of massive quiescent galaxies at Cosmic Noon, based on deep spectroscopy obtained by the Blue Jay survey using the NIRSpec instrument onboard JWST. In Section 2 we describe the spectroscopic data and the selection of the quiescent sample. In Section 3 we present the spectral fitting of the emission lines: the results derived from these fits are explored in Section 4, where we investigate the origin of the observed ionized gas using several line diagnostics, and in Section 5, where we derive upper limits on the current star formation rates. In Section 6 we conduct a more in-depth spectral analysis on a subset of galaxies which show signs of powerful ionized gas outflows and derive the outflow velocities. In Section 7 we gather all the evidence obtained from our data analysis to try and identify the main ionization mechanisms for this sample of $z \sim 2$ quiescent galaxies, and put our results in context within the overall picture of quenching in high-redshift systems.

2. DATA AND SAMPLE SELECTION

2.1. *The Blue Jay survey*

This work is based on spectroscopic data obtained by the Blue Jay survey, a medium-sized JWST Cycle-1 program (GO 1810; PI: S. Belli). Observations targeted 147 galaxies at Cosmic Noon and 4 filler galaxies at $z \sim 6$, for a total of 151 targets, and were performed using the NIRSpec instrument in multi-object mode with the Micro-Shutter Assembly (MSA). The targets were selected in the COSMOS field using Hubble Space Telescope (HST) observations by the Cosmic Assembly Near-Infrared Deep Extragalactic Legacy Survey (CANDELS; Grogin et al. 2011; Koekemoer et al. 2011) and the photometric catalog released by the 3D-HST team (Brammer et al. 2012; Skelton et al. 2014; Momcheva

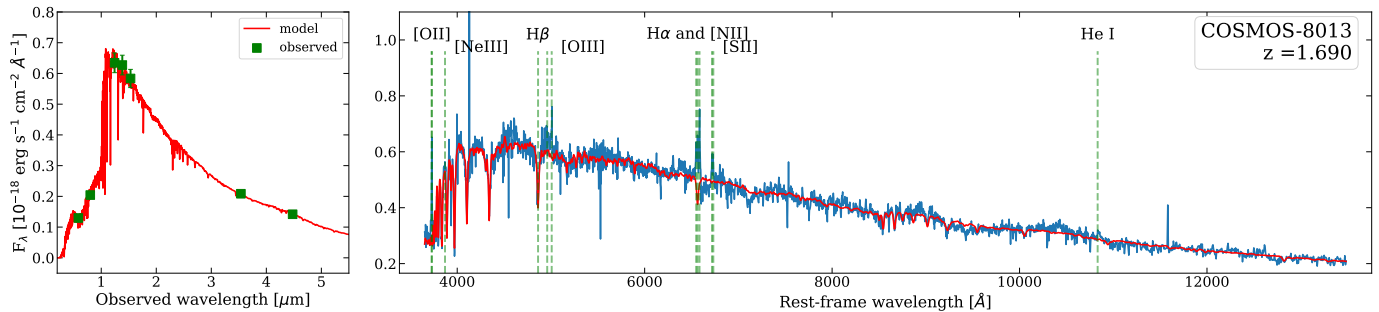


Figure 1. Example of stellar population fit for a quiescent galaxy. Left panel: photometric data (green squares) with the best-fit Prospector model (red line). Right panel: observed NIRSpect spectrum (blue) overlaid with the best fit from Prospector (red), adopting a wide wavelength range. Highlighted emission lines (green dashed lines) have been masked during the stellar continuum fit.

et al. 2016), which includes both ground- and space-based data. The target selection was designed to ensure a roughly uniform coverage in both redshift and stellar mass, yielding a representative sample of galaxies with stellar mass $9 \lesssim \log(M_*/M_\odot) \lesssim 11.5$ in the redshift range $1.7 < z < 3.5$.

Each target was observed through an MSA slitlet composed of at least two shutters. Empty shutters were used to construct a master background spectrum, which was then subtracted by each target spectrum. Targets were observed using the G140M/F100LP, G235M/F170LP and G395M/F290LP medium-resolution gratings ($R \sim 1000$) with exposure times of 13h, 3.2h and 1.6h respectively. The individual grating spectra were combined to produce spectra with a continuous wavelength coverage from 1 to 5 μm , but with occasional gaps due to the space between the two NIRSpect detectors. The full description of the Blue Jay survey design and data reduction process will be provided in the survey paper (Belli et al, in prep.).

2.2. Stellar continuum fit and flux calibration

In order to measure the emission line fluxes from the observed spectra, we need to account for two issues. First, given the small size of the MSA shutters, the NIRSpect spectra probe only a fraction of the light emitted by the target and are therefore affected by heavy slit losses: any line flux measured from the spectra will therefore underestimate the true line flux. Second, the spectra of massive galaxies typically have a strong stellar continuum, which must be subtracted from the observed spectrum to obtain the spectrum of the ionized gas. We solve both problems by fitting stellar population models to the combined photometric and spectroscopic data.

The fitting procedure and the analysis of the stellar population properties, including the star formation histories, are detailed in Park et al. (2024); here we only give a summary of the methodology. The fits were done using the fully Bayesian code **Prospector**

(Johnson et al. 2021), following the approach outlined in Park et al. (2023) and Tacchella et al. (2022). The **Prospector** code adopts the stellar population synthesis model FSPS (Conroy et al. 2009) and a set of free parameters to generate a synthetic galactic spectral energy distribution which can then be fitted to the observations. The model is highly flexible and includes a non-parametric star formation history fitted over 14 age bins, dust attenuation, and dust emission at longer wavelengths. A single **Prospector** model is fitted both to the NIRSpect spectrum, in which all the emission lines analyzed in this work are masked out, and to HST/ACS+WFC3 and Spitzer/IRAC (channels 1 and 2) photometric data from 3DHST (Skelton et al. 2014). During the fit, a polynomial distortion is applied to the spectrum in order to match it with the multi-band photometry. This method ties the flux calibration of the spectrum to that of the broadband photometry, which is far more robust; and it also accounts for slit losses if we assume that the emission probed by the MSA shutters is a scaled down version of the total emission coming from the whole galaxy, i.e., assuming spatially uniform emission across the target. We also assume that the ionized gas emission has the same distribution of the stellar emission, so that the same flux calibration can be applied to both components. In any way, this assumption does not significantly impact our results because they are mostly based on line ratios and equivalent widths.

For each galaxy, the Blue Jay spectra cover a wide wavelength range due to the use of three separate gratings. However, the default **Prospector** fits use only the rest-frame 4000-6700 \AA region, which is easier to model with synthetic stellar populations and is less prone to systematic uncertainties, since the calibration polynomial can artificially change the strength of the 4000- \AA continuum break. This choice leads to the most robust measurements of the galaxy physical properties (see Park et al. 2024). On the other hand, several emission lines from ionized gas lie outside this spectral region,

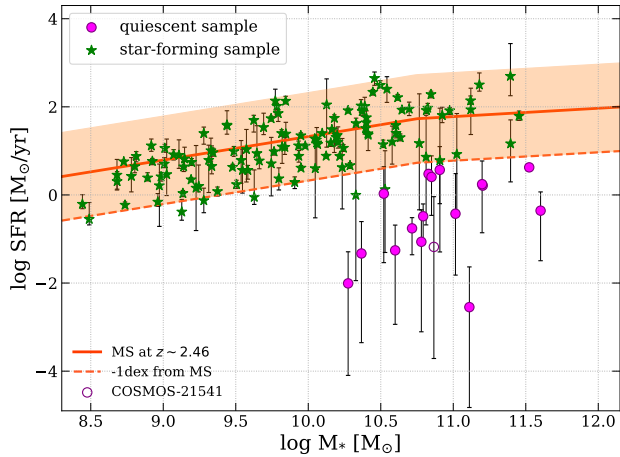


Figure 2. Stellar mass vs SFR (averaged over the last 30 Myr) for the Blue Jay sample. The orange solid line marks the star-formation main sequence at $z = 2.46$ from [Leja et al. \(2022\)](#); the orange shaded region shows the ± 1 dex limits.

and so **Prospector** was run again on a wider wavelength range, from 3700 to 13700 Å; see Figure 1 for an example. Both versions of the **Prospector** fit use the same set of broadband photometry and adopt the same model. In the present work, we take the physical measurements such as stellar mass and star formation rate from the default fits with a narrow wavelength range, but we adopt the fits with extended wavelength range when measuring the emission lines.

2.3. Quiescent sample selection

To select the quiescent galaxies from the parent sample, we adopt the SFR-based selection of [Park et al. \(2024\)](#). Using the star formation history derived with **Prospector**, we take the mean SFR over the last 30 Myr as the “instantaneous” measurement, and compare it to the main sequence of star-forming galaxies measured by [Leja et al. \(2022\)](#) at each galaxy’s redshift. We then classify as quiescent those galaxies whose 84th percentile of the SFR posterior distribution lies more than 1 dex below the main sequence. We further exclude one galaxy (COSMOS-21541) since the data reduction of its NIR-Spec spectrum failed. We thus obtain a sample of 16 quiescent galaxies, represented by the magenta circles in Figure 2, which illustrates the SFR vs stellar mass diagram of the whole Blue Jay sample, as well as the [Leja et al. \(2022\)](#) star-formation main sequence at $z \sim 2.46$ (median redshift of the Blue Jay sample) plotted for visual reference. The main properties of the quiescent sample are listed in Table 1; we note that all the selected galaxies are more massive than $10^{10.2} M_{\odot}$.

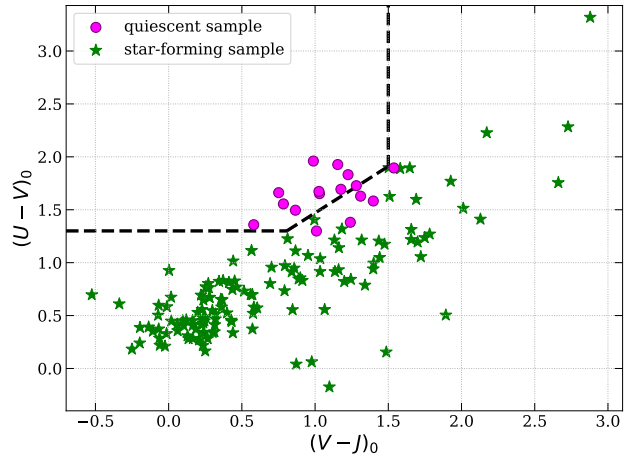


Figure 3. The Blue Jay sample on the UVJ diagram. Dashed black lines mark the [Muzzin et al. \(2013\)](#) selection of quiescent galaxies.

2.4. Alternative sample selection

We check our selection by plotting the sample onto the rest-frame UVJ color-color diagram (Figure 3), which has been proven effective in selecting quiescent galaxies up to $z = 3.5$ ([Williams et al. 2009](#); [Whitaker et al. 2011](#); [Straatman et al. 2016](#)). We calculate the rest-frame colors using the public photometric redshift $EAzY$ code ([Brammer et al. 2008](#)), and adopting the UV-to-NIR photometry from the 3D-HST catalog, to which we add near-infrared photometry measured on JWST/NIRCam data from the PRIMER survey ([Dunlop et al. 2021](#)). The rest-frame $U - V$ and $V - J$ colors are reported in Table 1.

As expected, most of the selected galaxies are found inside the quiescent selection limit at $z > 1$ ([Muzzin et al. 2013](#)), traced by the black dashed line, with some galaxies found just outside the boundary. A criterion based purely on the UVJ colors would have selected a subset of our sample (see also discussion in [Leja et al. \(2019\)](#) and [Tacchella et al. \(2022\)](#)); the SFR-based selection can therefore be considered slightly broader. Given that the two types of selection result in similar samples, we conclude that our results could also be applied to a sample of color-selected quiescent galaxies for which no spectroscopy is available.

3. SPECTRAL FITTING

We employ the wide-range **Prospector** fits (§ 2) to subtract the stellar contribution from the spectra and isolate the emission due to ionized gas. We then construct a model for the ionized gas spectrum, composed of a Gaussian profile for each of the emission lines listed

Table 1. Overview of selected quiescent galaxies properties

COSMOS ID	H mag	Rest-frame colors		Prospector fitted parameters		
		$U - V$	$V - J$	z	$\log M_*/M_\odot^a$	SFR (M_\odot/yr)
7549	24.3	2.0	1.3	2.627	10.82	$3.0^{+0.7}_{-0.7}$
8013	22.2	1.5	0.7	1.690	10.54	1^{+3}_{-1}
8469	22.7	1.5	1.0	1.868	10.58	$0.06^{+0.15}_{-0.05}$
9395	22.6	1.6	0.7	2.127	10.70	$0.2^{+0.1}_{-0.1}$
10128	21.9	2.0	1.2	1.852	11.16	$1.6^{+0.3}_{-0.3}$
10339	23.7	1.7	0.7	2.363	10.34	$0.05^{+0.20}_{-0.05}$
10400	24.1	2.2	1.1	2.099	10.27	$0.01^{+0.04}_{-0.01}$
10565	23.3	1.8	1.0	2.441	10.80	$0.3^{+0.3}_{-0.2}$
10592	21.7	1.8	1.0	1.801	11.10	$0.00^{+0.02}_{-0.00}$
11142	22.7	1.7	1.0	2.444	10.90	4^{+9}_{-3}
11494	20.8	1.9	1.0	2.091	11.65	$0.4^{+0.7}_{-0.4}$
16419	21.1	1.6	1.0	1.925	11.51	$4.2^{+0.9}_{-0.7}$
18668	22.9	1.9	1.5	2.086	11.01	$0.4^{+2.7}_{-0.4}$
18688	21.8	1.6	1.2	2.007	11.18	2^{+4}_{-2}
19572	22.3	1.2	1.0	1.867	10.86	3^{+5}_{-2}
21477	22.6	1.4	0.7	2.474	10.76	$0.09^{+0.37}_{-0.09}$

^aTypical error on stellar mass 0.05 dex.

Table 2. Fitted emission lines

Species	$\lambda_{rest-frame}$ (Å)
[OII]	3727.10, 3729.86
[NeIII]	3869.86
H β	4862.71
[OIII]	4960.30, 5008.24
[NII]	6549.86, 6585.27
H α	6564.60
[SII]	6718.29, 6732.67
He I	10833.31

NOTE—Rest-frame wavelength in vacuum.

in Table 2. Given the relatively low spectral resolution of the observations and the fact that we are observing gas-poor, quiescent galaxies, we adopt a single kinematic component with the same velocity dispersion and redshift for all the lines in each galaxy. As will be explored in § 6, these assumptions do not hold up for all galaxies in the sample. The flux ratios between [OIII]5007/[OIII]4959 and [NII]6581/[NII]6548

are fixed at the theoretical value of 3:1, following [Osterbrock & Ferland \(2006\)](#). Although our spectral resolution is not sufficiently high to be able to resolve the [OII] $\lambda\lambda$ 3727,3739 doublet, we fit the lines separately and impose the $1.5 < [\text{OII}]3729/[\text{OII}]3727 < 2.5$ theoretical limit on their flux ratio ([Osterbrock 1989](#)). The velocity dispersion parameter is fitted taking into account the contribution to the overall broadening of the lines given by the wavelength-dependent NIRSspec nominal spectral resolution.

The fitting is performed using the EMCEE Python library, an Affine Invariant Markov Chain Monte Carlo (MCMC) Ensemble sampler ([Foreman-Mackey et al. 2013](#)). We cut spectral regions of width 600 Å in the observed frame around each emission line and fit only the data within these regions. The free parameters of the model are the global redshift z_{gas} and velocity dispersion σ_{gas} (identical for all lines), and the flux of each line (apart from lines with a fixed flux ratio). Flux and velocity dispersion priors are constructed by employing flat logarithmic probability distributions, in order to represent our ignorance of the real probability distribution of these parameters. The velocity dispersion prior is set between 10 and 1000 km/s. For the redshift parameter we adopt a Gaussian prior, centered around the Prospector-estimated value, with dispersion informed by the Prospector posterior distribution for z . The re-

sulting best-fit emission line parameters are determined as the median values from the EMCEE posterior distribution, with uncertainties calculated as the values at the 16th and 84th percentile ranges, and are reported in Appendix A.

As already discussed in Section 2.2, a correction is applied to the spectra in order to align the spectroscopic flux with the measured photometry. Assuming that the ionized gas emission is originating mainly in HII regions scattered throughout the galaxy, the slit-loss calibrated spectrum yields accurate flux estimations. However, it is possible that emission in these quiescent galaxies comes from limited regions of ionized gas that are not evenly distributed throughout the galaxy, e.g. only the nuclear regions: in this case, slit-loss flux corrections may not be accurate and fluxes may be overestimated.

4. IONIZED GAS CONTENT OF QUIESCENT GALAXIES

The deep JWST/NIRSpec data obtained by the Blue Jay survey reveals the widespread presence of ionized gas in the quiescent galaxy population. Figure 4 illustrates the HST cutouts and NIRSpec data for each galaxy. The continuum-subtracted data are shown in blue, while the best-fit spectrum obtained from the MCMC fitting is traced by the red solid line, with the red shaded regions indicating the 1σ , 2σ and 3σ confidence levels. We detect at least one emission line with $\text{SNR} > 3$ – formal limit of line detection for this work – in 12 out of 16 galaxies (75% of the sample); and for most galaxies we find that multiple emission lines are robustly detected. This surprising result suggests the presence of continued ionizing sources in the population of quiescent galaxies at $z \sim 2$. Formally, only two spectra (IDs 10400 and 21477) out of 16 show no detected emission lines. However, we notice that the spectra of galaxies COSMOS-10592 and COSMOS-8469 appear to suffer from the presence of systematics in the data: thus, the formal line detections we have for these galaxies are not reliable, and we treat them as non-detections. Furthermore, we find that galaxy COSMOS-11494, the most massive in the sample, shows few emission lines that are formally detected but at very low SNR. Low SNR and non-detections characterize the noisiest spectra of the sample: in many of these cases, the MSA slits appear to be not well-centered on their galaxies: this could be a factor contributing to the missing detections of emission lines in these systems. In fact, the mean flux correction applied to the spectra due to slit loss is of a factor ~ 2 , while for the low SNR galaxies the corrected flux averages at around 4 times the observed flux.

Lines detected with the highest SNR in the sample are low-ionization lines, such as the [OII] doublet at $\lambda 3727, 2729\text{\AA}$ and $\text{H}\alpha$, while higher ionization lines such as [OIII] $\lambda 5007$ are more rarely detected. The [NeIII] line, a high-ionization line which is considered to be a tracer of AGN emission, is successfully detected in only two galaxies (COSMOS-11142 and COSMOS-18688) and is thus not included in Figure 4. The He I line, which is a high-ionization line usually not detected in quiescent galaxy’s spectra even at low- z , is actually detected with $\text{SNR} > 3$ in 7 galaxies of the sample and is further discussed in Section 6.3.

4.1. Emission line ratios

From Figure 4 it is clear that, for most galaxies, the [NII] $\lambda 6783$ line is similar to, or stronger than, the $\text{H}\alpha$ line. A high [NII]/ $\text{H}\alpha$ line ratio is indicative of a hard ionizing photon field, typical of AGN or shock-induced photoionization (Kewley et al. 2019), even though it is also influenced by metallicity. In Figure 5, we show the [NII]/ $\text{H}\alpha$ ratio of the star-forming and quiescent galaxies in the Blue Jay sample, as a function of their position on the UVJ diagram: most of the galaxies in the quiescent sample tend to have [NII]/ $\text{H}\alpha$ ratio equal or higher than 1, while much lower values are typical of the star-forming sample. We also notice a trend in [NII]/ $\text{H}\alpha$ ratio along the star-forming population, where redder galaxies tend to have higher values of the [NII]/ $\text{H}\alpha$ ratio. This is likely due to the underlying correlation between color and mass: redder star-forming galaxies are more massive and thus contain more dust. Massive star-forming galaxies, in turn, have higher metallicity, resulting in a higher [NII]/ $\text{H}\alpha$ ratio. Moving towards the quiescent part of the diagram, however, we find generally higher [NII]/ $\text{H}\alpha$ ratios compared to star-forming galaxies, suggesting a more complex origin behind the observed line ratio.

In order to explore the origin of the ionization, in Figure 6 we show the Blue Jay sample on the [NII]/ $\text{H}\alpha$ vs. [OIII]/ $\text{H}\beta$ diagram, i.e., the so-called BPT diagram (Baldwin et al. 1981). We consider galaxies where all four emission lines ([NII] $\lambda 6583$, $\text{H}\alpha$, [OIII] $\lambda 5007$, and $\text{H}\beta$) are detected with $\text{SNR} > 3$; in order to include as many galaxies as possible from the quiescent sample, we also plot upper/lower-limit values at 3 sigma for systems with at least one detection at $\text{SNR} > 3$ in each of the two line ratios. Examples of galaxies added this way are COSMOS-8013 and COSMOS-16419. The distribution of the two samples on the diagram is compared with the observationally-derived star formation limit by Kauffmann et al. (2003), based on local SDSS galaxies, and the theoretical limit of extreme starburst

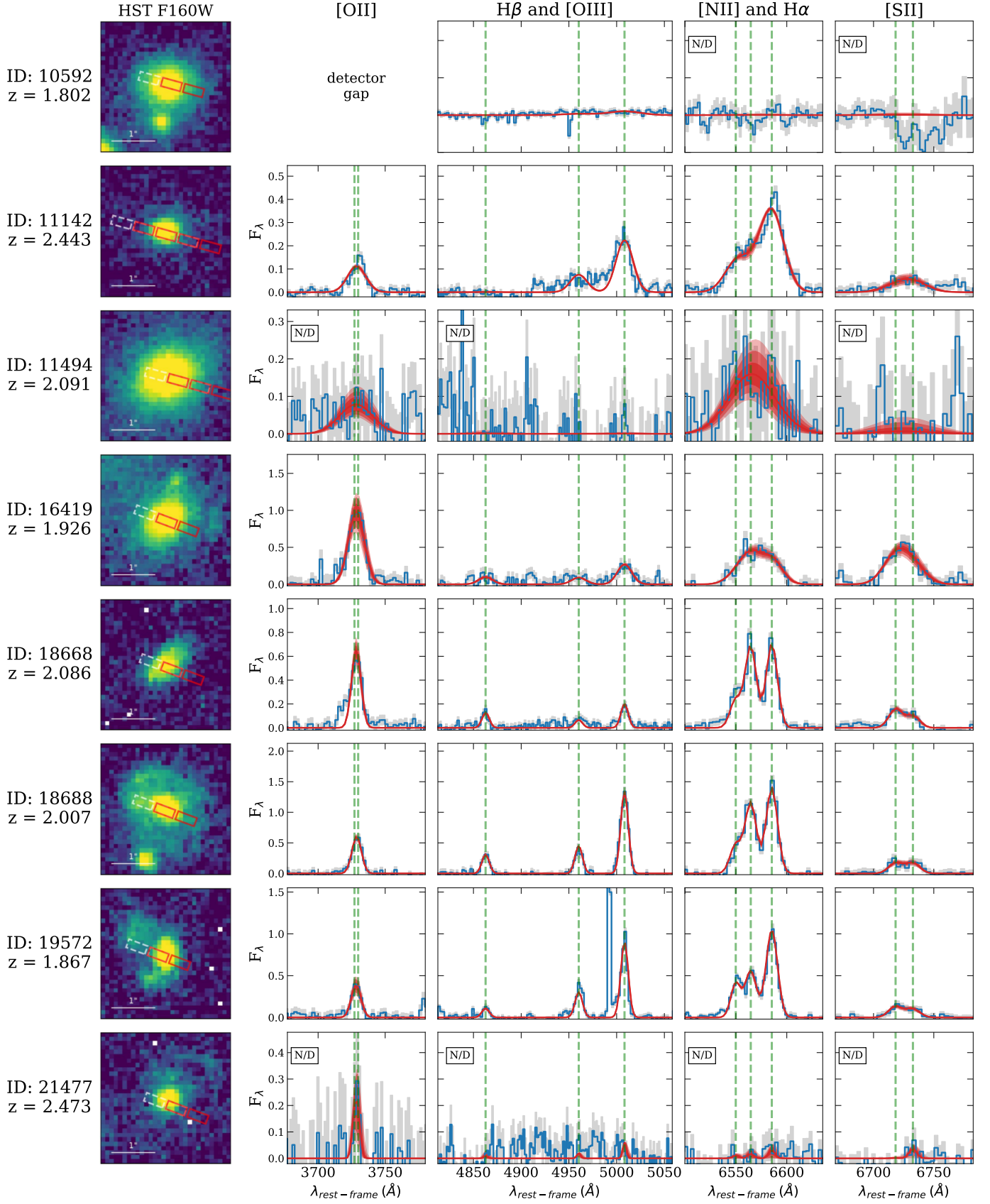


Figure 4. Cutouts and observed spectra for the sample of quiescent galaxies in the Blue Jay survey. The $3'' \times 3''$ cutouts are from HST F160W imaging, and the footprint of the MSA shutters is shown in red and white for the A and B nod positions, respectively. In the remaining panels, the observed spectrum is in blue, with the 1σ uncertainty marked by the shaded grey region. Flux is in units of $10^{-18} \text{ erg s}^{-1} \text{ cm}^{-2} \text{ \AA}^{-1}$. The red line and shaded regions show the median and the $\pm 1, 2, 3\sigma$ confidence regions for the results of the emission line fit. Panels where emission lines are not detected are labeled with "N/D". The reported redshifts are derived from the emission line fits.

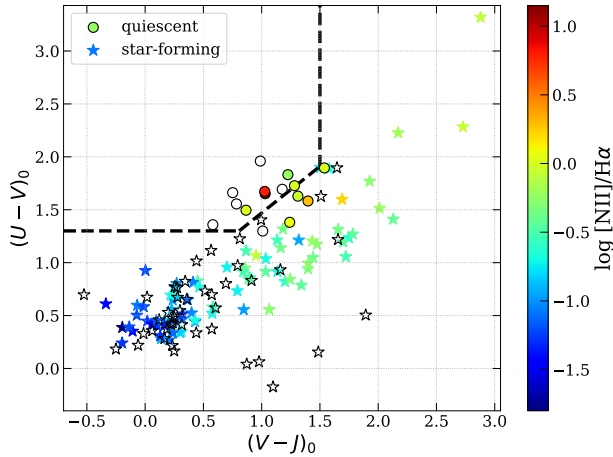


Figure 5. Blue Jay sample on the UVJ diagram. The symbol shape indicates the SFR-based selection of quiescent galaxies, while the color coding shows the measured $[\text{NII}]/\text{H}\alpha$ line ratio. An empty marker means that $[\text{NII}]\lambda 6583$ and $\text{H}\alpha$ are not detected with $\text{SNR} > 3$.

galaxies by Kewley et al. (2001). The empirical classification of the AGN population into Seyfert and LINERs given by Kewley et al. (2006) is shown as well. We find a clear segregation of the quiescent Blue Jay sample on the AGN-powered side of the diagnostic diagram, excluding one object (COSMOS-7549) which is instead found inside the extreme starburst limit, in the lower part of the diagram. This galaxy has non-detected $[\text{OIII}]$ line, which translates into an upper limit on the $[\text{OIII}]/\text{H}\beta$ ratio which is much lower than what is found among the rest of the sample.

The star-forming galaxies in the Blue Jay sample form a well defined sequence along the so-called star forming galaxy abundance sequence (Kewley et al. 2006). This sequence is slightly shifted towards higher $[\text{OIII}]/\text{H}\beta$ ratios compared to the distribution of local galaxies, which we take from the MPA-JHU DR7 release¹ of spectral measurements for the SDSS survey (Tremonti et al. 2004). This is a well-known phenomenon observed at Cosmic Noon (Strom et al. 2017; Kewley et al. 2019), and is likely due to lower-metallicity and α -enhanced stellar populations (Sanders et al. 2020; Steidel et al. 2016). Despite this offset, the quiescent sample remains well-separated from the star-forming sequence, indicating that the primary ionizing source present in these galaxies is not star-formation, but rather the probable presence of an active galactic nucleus. This conclusion is further reinforced by the $[\text{SII}]/\text{H}\alpha$ (Veilleux & Os-

terbrock 1987) and $[\text{OIII}]/[\text{OII}]$ (not corrected for dust) (Dopita et al. 2000) diagnostic diagrams, shown in Figure 7 and Figure 8: again, the quiescent sample is mostly found to the right of the maximum starburst limit, confirming that a surprising number of these galaxies may be hosting an AGN in their center. Interestingly, the star-forming galaxies (selected by their SFR) that are found on the AGN side of the diagnostic diagrams are a very small fraction of the total. Two of these AGN-hosting star-forming galaxies are COSMOS-18977 and COSMOS-12020, which are the only two spectroscopically confirmed Broad Line AGN in the Blue Jay sample (see Figure 6).

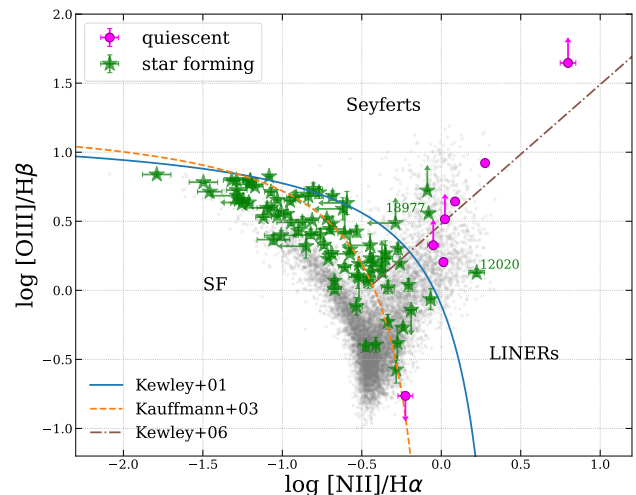


Figure 6. BPT diagram for the Blue Jay sample. Galaxies classified as quiescent from their SFR are shown with magenta circles. Among the star-forming population (green stars), the two broad line AGNs COSMOS-18977 and COSMOS-12020 are highlighted. The gray points are local galaxies from the SDSS (Tremonti et al. 2004).

4.2. $\text{H}\alpha$ equivalent width

We also make use of the WHaN diagnostic diagram introduced by Cid Fernandes et al. (2010, 2011) (CF10, CF11). This line diagnostic diagram is similar to the BPT diagram, but with the $[\text{OIII}]/\text{H}\beta$ line ratio replaced by the $\text{H}\alpha$ equivalent width, which is easier to obtain in low-SNR spectra, thus allowing us to plot more quiescent galaxies with respect to the BPT. The results of the WHaN diagram, shown in Figure 9, are consistent with those of the BPT diagram: we find most of the quiescent sample clustered on the AGN region of the plot. As before, the exception is COSMOS-7549, which is classified as a composite galaxy, as well as COSMOS-10565, which is the only one to be found in the "retired galaxies" region. When compared with

¹ Online repository: <https://wwwmpa.mpa-garching.mpg.de/SDSS/DR7/#platablelist>

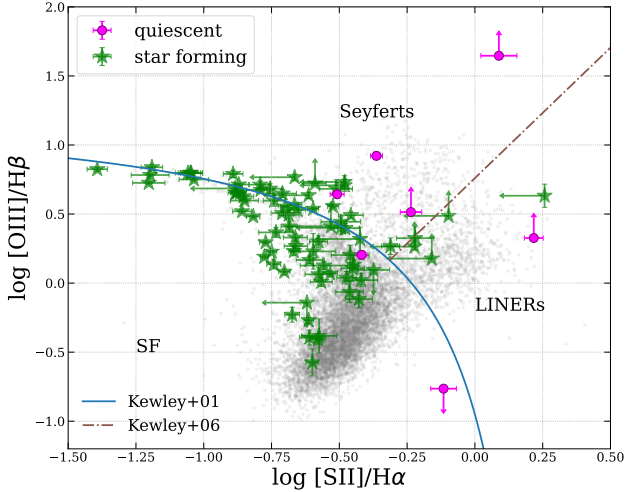


Figure 7. $[\text{OIII}]/\text{H}\beta$ vs $[\text{SII}]/\text{H}\alpha$ diagram. Symbols as in Figure 6.

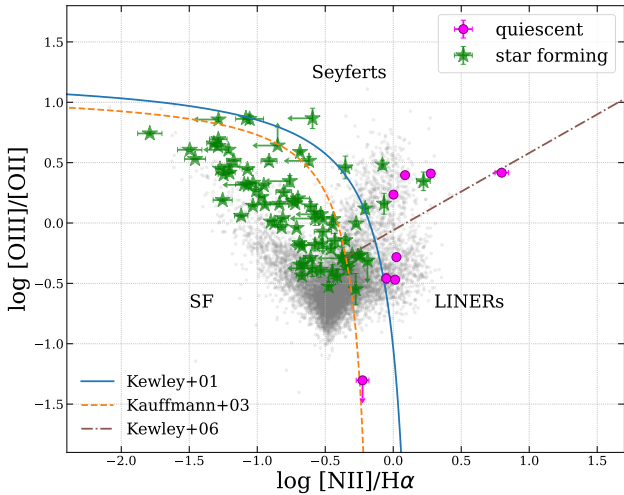


Figure 8. $[\text{OIII}]/[\text{OII}]$ vs $[\text{NII}]/\text{H}\alpha$ diagram. Symbols as in Figure 6.

the population of SDSS galaxies at $z = 0$, the distribution of the star-forming sample is systematically shifted towards higher $\text{H}\alpha$ EWs, as observed also by Belli et al. (2017) at $0.7 < z < 2.7$: this shift can be attributed to the elevated specific SFR typical of Cosmic Noon galaxies (Madau & Dickinson 2014), which naturally results in a higher $\text{H}\alpha$ EW.

The WHaN diagram is very effective in distinguishing between low-power AGNs and weak Emission Lines Retired Galaxies (EL-RGs) (CF11). In retired galaxies the ionizing flux comes from hot evolved post-AGB stars (Stasińska et al. 2006), but due to the hard ionizing field these galaxies are often misclassified by the BPT diagram. To differentiate between true AGN and

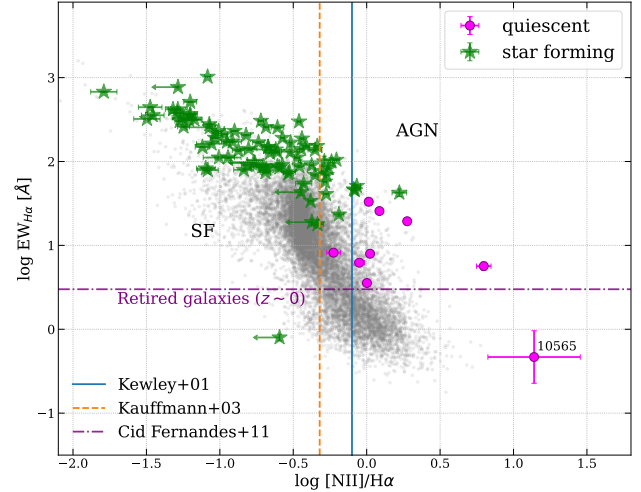


Figure 9. WHaN diagram for the Blue Jay sample. Symbols as in Figure 6.

retired galaxies, CF11 propose a division on the WHaN diagram at $\text{EW}(\text{H}\alpha) = 3 \text{ \AA}$. In our sample, only one galaxy (COSMOS-10565) falls below this line. However, we have to consider that the limit set at 3 \AA by CF11 has been calibrated on local galaxies and may not hold up at higher redshift. The quiescent galaxies observed by Blue Jay are substantially younger than those observed at $z \sim 0$ (many of them have stellar ages ≤ 1 Gyr, see Park et al. 2024), since the age of the Universe at $z \sim 2$ is only 3 Gyr, and photoionization models show that the LIERs-like (Low-Ionization Emission Regions) line emissions due to post-AGB stars are actually weaker in younger stellar populations (Byler et al. 2019). This means that the $\text{H}\alpha$ emission by retired galaxies at Cosmic Noon must be even fainter than the $\text{EW} = 3 \text{ \AA}$ limit set by CF11. We thereby conclude that this type of ionization is not relevant for the vast majority of galaxies considered in this study.

4.3. Line kinematics

As a last piece of the puzzle, in Figure 10 we show the relation between the $[\text{NII}]/\text{H}\alpha$ line ratio and σ_{gas} , the velocity dispersion measured from the emission lines, for both the quiescent and the star-forming population. We find a clear division of the two samples, mirroring the division found in the other diagnostic diagrams: the quiescent sample is characterized by a higher $[\text{NII}]/\text{H}\alpha$ ratio and a higher gas velocity dispersion with respect to the star-forming sample. In many cases the velocity dispersion is so large ($\sigma_{\text{gas}} > 400 \text{ km/s}$) that it is clearly not due to the galaxy gravitational potential, but it must trace other processes such as outflows or shocks (Rich et al. 2011, 2014), which must be associated to AGN activity (as discussed below). As a note, when fitting the

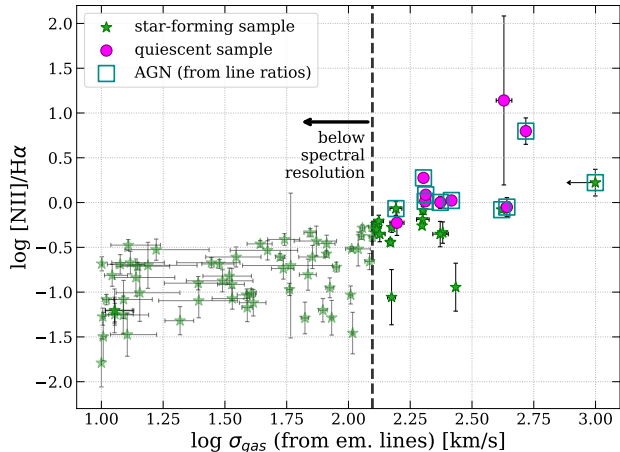


Figure 10. Comparison of the $[\text{NII}]/\text{H}\alpha$ ratio and the velocity dispersion of emission lines for the Blue Jay sample. Empty squares mark galaxies identified as AGN on the BPT diagram. For the broad-line AGN COSMOS-12020 we can only measure an upper limit on the velocity dispersion.

velocity dispersions we adopted the nominal spectral resolution provided by JDox: however, we stress that the actual spectral resolution may be higher than this for compact sources (see de Graaff et al. 2024), thus the velocity dispersion values we provide may be underestimated. This issue mainly affects galaxies near or below the nominal spectral resolution, which is marked by the dashed black line in Figure 10, and is not relevant for galaxies with high measured velocity dispersion. We also highlight with blue square frames the galaxies that are AGN hosts according to the diagnostic diagrams: notably, star-forming AGN hosts are found mixed in with the quiescent sample. Our analysis of the kinematics further confirms the AGN origin of the observed emission in quiescent galaxies.

4.4. AGN activity in the sample

The classification of galaxies in the sample based on their rest-frame optical lines is summed up in Table 3. We are able to classify 9 out of 16 galaxies (56%), while the rest of them are either missing the required emission lines altogether or they have too low SNR for the diagrams to be reliable. Only one galaxy, COSMOS-7549, is classified as part of the composite population: this system completely lacks any $[\text{OIII}]$ emission and may be a recently quenched non-active galaxy, whose residual ionizing flux from A-type stars is enough to produce low-ionization emission lines, such as $[\text{OII}]$ and $\text{H}\alpha$, but no young stellar population is present to doubly ionize oxygen. This is similar to the sample of $[\text{OIII}]$ -deficient galaxies analyzed by Quai et al. (2018) at $z < 0.21$; we further explore the star formation history of this system

in Section 5. Another galaxy, COSMOS-10565, is the only one classified as a retired galaxy by the WHaN diagram and could be a genuine inactive quiescent galaxy. However, its extreme $[\text{NII}]/\text{H}\alpha$ ratio and the presence of neutral gas outflows, as reported by Davies et al. (2024), suggest a more complex reality. This specific system is further discussed in Section 6.

Most importantly, all the other galaxies reveal signs of hosting an AGN in their center. AGN represent 78% of the quiescent galaxy population for which we have reliable classification from line ratios, corresponding to a global 44% of all galaxies in the quiescent sample. The incidence of AGN in our sample is comparable to the one found by Förster Schreiber et al. (2019) in gas-rich, massive star-forming galaxies at Cosmic Noon. However, this high incidence is not necessarily expected for gas-poor quiescent galaxies, such as the ones in our sample. These sources are not classified as AGN by any other catalog. None of these galaxies are detected in the X-rays by either the Chandra-COSMOS Legacy Survey Point Source Catalog (Civano et al. 2016) or the COSMOS XMM Point-like Source Catalog (Cappelluti et al. 2009). Only one object (COSMOS-18688) is detected in the radio by the VLA-COSMOS 3 GHz Large Project and COSMOS VLA Deep surveys (Smolčić et al. 2017; Schinnerer et al. 2004). The AGN properties of the sample are discussed further in Section 7.1.

One caveat is that the BPT and other rest-frame optical diagnostic diagrams cannot discriminate between shocks and AGN photoionization: Dopita & Sutherland (1995) and Ho et al. (2016) showed that diffuse radiation produced by fast shocks ($v_{gas} \sim 150 - 500$ km/s) from jets or star-formation feedback can reproduce optical emission line ratios of both LINERs and Seyfert galaxies. We are not able to rule out the possibility that shocks, rather than AGN photoionization, may play a dominant role in the excitation budget of the quiescent sample. However, even if fast shocks were present in these quiescent galaxies, some of these quiescent galaxies also show outflows (see Section 6) which cannot be star-formation-driven given the low SFR measured in these systems (see Section 5). Moreover, only one galaxy classified as AGN, COSMOS-19572, seems to be a merging system (see again Section 6); for the other galaxies we can thus exclude that the shocks are a consequence of galaxy interactions. The only possible source of shocks for the bulk of BPT-classified AGN, then, is through mechanical feedback from the AGN itself.

5. STAR FORMATION RATE

Table 3. Quiescent sample classification and SFR from H α line luminosity

ID	BPT	WHaN	[OIII]/[OII]	[SII]/H α	A $_v$ (mag)	SFR (M $_{\odot}$ /yr)
7549	SF/Comp.	SF/Comp.	Comp.	SF	$-0.05^{+0.07}_{-0.08}$ *	$0.145^{+0.002}_{-0.003}$
8013	Seyfert	AGN	LINER	Seyfert	$1.4^{+0.5}_{-0.3}$	$2.0^{+1.8}_{-0.7}$
8469	—	—	—	—	$0.9^{+0.4}_{-0.3}$	< 0.06
9395	—	—	—	—	$0.8^{+0.3}_{-0.2}$	< 0.14
10128	—	AGN	Seyfert	—	$1.4^{+0.4}_{-0.3}$	$0.6^{+0.3}_{-0.2}$
10339	—	—	—	—	$1.5^{+0.4}_{-0.3}$	—
10400	—	—	—	—	$0.2^{+0.3}_{-0.1}$	< 0.02
10565	—	EL-RG	—	—	$1.3^{+0.4}_{-0.3}$	$0.1^{+0.1}_{-0.1}$
10592	—	—	—	—	$0.3^{+0.2}_{-0.2}$	< 0.001
11142	Seyfert	AGN	LINER	Seyfert	$2.4^{+0.5}_{-0.4}$	$5.6^{+4.9}_{-2.5}$
11494	—	—	—	—	$0.7^{+0.2}_{-0.2}$	$2.6^{+1.1}_{-0.8}$
16419	LINER	AGN	LINER	LINER	$0.4^{+0.2}_{-0.1}$	$1.9^{+0.5}_{-0.3}$
18668	LINER	AGN	LINER	SF	$3.04^{+0.12}_{-0.13}$ *	45^{+5}_{-6}
18688	Seyfert	AGN	Seyfert	Seyfert	$1.90^{+0.06}_{-0.06}$ *	19^{+1}_{-1}
19572	Seyfert	AGN	Seyfert	Seyfert	$2.81^{+0.12}_{-0.13}$ *	24^{+3}_{-4}
21477	—	—	—	—	$1.3^{+0.4}_{-0.5}$	< 0.3

*Dust attenuation derived from Balmer ratio

NOTE—Classification of the sample according to various diagnostic diagrams and SFR estimates from H α line luminosity. Upper limits for SFR at the 3σ confidence level are given for galaxies without H α detection. Galaxy 10339 has no H α line due to a detector gap.

We derive the SFR of each galaxy in the sample from the H α line luminosity, assuming the conversion provided by Kennicutt (1998). However, the conversion of H α luminosity to SFR is affected by several issues. First, we know from the emission line ratios that most of the H α emitters in the quiescent sample host an AGN, which is clearly the greatest contributor to the measured H α flux. In these cases, we consider the calculated SFRs as strict upper limits. Secondly, the measured line fluxes are affected by slit loss. This effect has been accounted for by the parametric correction estimated by *Prospector* and applied to the spectra before fitting the emission lines (see § 2): as already mentioned in § 3, however, the calibrated H α line luminosity is overestimated in the case of ionized gas emission whose origin is not evenly distributed throughout the galaxy. Finally, the measured line fluxes are affected by dust attenuation. Ideally, we would use the H β /H α Balmer decrement to estimate the nebular dust attenuation: in most cases, however, the SNR of the H β line is too low. We therefore choose to estimate the attenuation A_V using the results of the *Prospector* fits. The dust attenuation curve

adopted by *Prospector* employs a two-components dust model (Charlot & Fall 2000) consisting of a dust optical depth associated with diffuse ISM dust, plus an additional dust component associated with dense star-forming clouds. *Prospector* further models dust extinction using a power-law modifier δ to the Calzetti et al. (2000) dust extinction law, following the empirical relation found in Kriek & Conroy (2013). Thus, we first employ the fitted two-component dust attenuation curve to derive the V-band extinction A_V and then obtain the dust-corrected H α flux applying the modifier δ estimated by *Prospector* to the Calzetti law.

The SFR estimates based on the H α line luminosity for the quiescent sample are summarized in Table 3. In four cases we are able to recover the dust correction from the H α /H β ratio and then apply the Calzetti law directly, in all the other instances we use the *Prospector* dust model. Figure 11 depicts the position of the Blue Jay galaxies in the stellar mass vs SFR diagram, with the SFR of the star-forming sample computed in the same way. Galaxies hosting an AGN according to the line diagnostic diagrams are highlighted with black

empty squares: for these cases, the computed SFR represents an upper limit. We find results in agreement with the initial SFR vs stellar mass selection plot, which was based on *Prospector* measurements (Figure 2). This confirms that the sample is indeed quiescent and lies well below the star formation main sequence at $z \sim 2$. Notably, three galaxies (IDs 18668, 18688, and 19572) exhibit SFR values higher than *Prospector* estimates, falling within ± 1 dex from the main sequence limit. However, given their status of AGN hosts, the measured H α emission predominantly originates from the active nucleus rather than star-forming regions, and thus their true SFR is lower than what measured from H α . Interestingly, one AGN within the star-forming sample, COSMOS-18977 ($z = 2.08$, $\log(M_*/M_\odot) = 10.70$), also borders the -1dex limit: this system is one of the two Broad Line AGN in the Blue Jay sample, as indicated by the large broadening of its permitted emission lines. Consequently, the stellar-continuum *Prospector* fit was performed only on the observed photometry (Park et al. 2024) and the estimated SFR may not be as accurate as for galaxies with a spectroscopic fit. In any case, we find a relatively low upper limit on its SFR from the H α line luminosity (SFR $\sim 18 M_\odot/\text{yr}$): given that the central AGN contributes significantly to the H α emission, and considering the presence of deep Balmer absorption lines in its spectrum, COSMOS-18977 could represent an additional massive quiescent galaxy hosting an AGN.

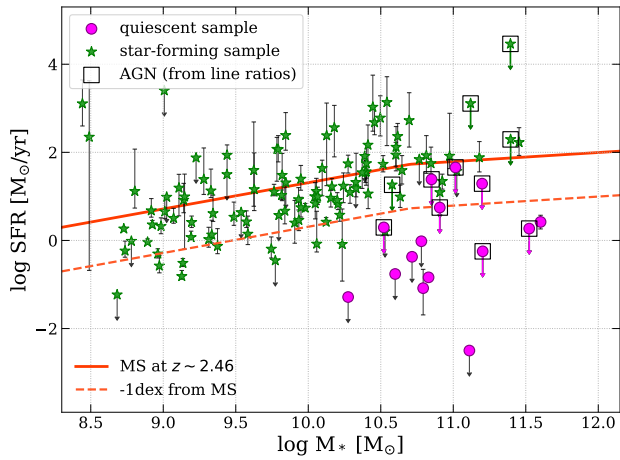


Figure 11. SFR from H α luminosity vs stellar mass for the Blue Jay sample. The orange solid line marks the star formation main sequence at $z = 2.46$ from Leja et al. (2022); the orange dashed line shows the -1 dex limit. Empty squares mark galaxies classified as AGN hosts by the diagnostic diagrams. Black upper limit arrows are used for H α non-detections, while colored arrows indicate AGN contamination.

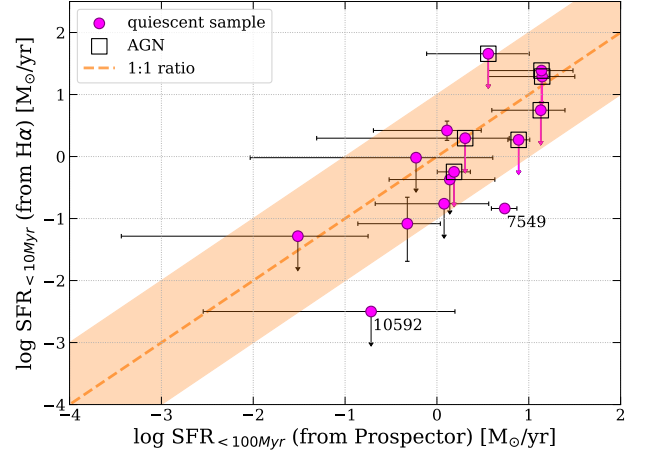


Figure 12. Comparison between the SFR computed on two different timescales: on a ~ 10 Myr scale using H α , and on a ~ 100 Myr scale using *Prospector*.

5.1. Rejuvenated candidates

The two SFR estimates of Table 1 and Table 3 trace the star formation activity of galaxies on different timescales. The *Prospector* measurement corresponds to the SFR in the most recent bin in the SFH posterior distribution, which spans the last 30 Myr of the galaxy history. The stellar continuum, however, is not sensitive to changes in the stellar population on such short timescales. Moreover, the SFH fits employ a “continuity” Bayesian prior on the SFR between adjacent time bins, which disfavors abrupt changes in the SFH such as bursts, quenching and rejuvenation events on short timescales. On the other hand, the SFR estimated from the observed H α line luminosity traces very recent star formation activity, since most of the H α flux in HII regions is due to short-lived massive stars, which photoionize the ISM around them on a time scale of ~ 10 Myr.

In Figure 12 we compare the SFR measured with the two methods, in order to explore the possibility of *rejuvenating* galaxies, i.e., galaxies that show recent star formation activity traced by H α but not detected by the *Prospector* fits. Because of the reasoning above, we choose to compute the *Prospector* SFR as the mean value over the last ~ 100 Myr as obtained by the reconstructed SFH. We find only two obvious outliers in the SFR-SFR plot, with most galaxies found within 1 dex of a 1-1 relation between the two estimates (orange shaded region). One of the outliers is galaxy COSMOS-10592, whose spectrum suffers from systematic errors in the data reduction and for which we cannot trust the computed quantities. Apparently, no clear rejuvenated candidates are found in the sample, because no galaxy ap-

pears to have increased significantly its SFR in the last ~ 10 Myr.

However, the second outlier, COSMOS-7549, may be of interest to understand variations of SFR on short timescales. This system is located at the highest redshift end of the sample ($z \sim 2.6$) and is the only galaxy classified as part of the composite population by the diagnostic diagrams, meaning that its observed emission line ratios could be produced by a mix of recent SF and a contribution from a weak active nucleus or shocked gas emission. Thus, we would expect to observe a slightly higher SFR from $H\alpha$ in this system with respect to the others, but instead we find a very low rate of $0.145 M_{\odot}/\text{yr}$ — one of the lowest of the sample. Furthermore, its $H\alpha$ -estimated SFR is much lower than the **Prospector**-estimated one, suggesting that the galaxy underwent rapid quenching sometimes between ~ 100 and ~ 10 Myr ago. According to the SFH fits of [Park et al. \(2024\)](#), when using a “bursty” prior for the **Prospector** fits — a modified prior which allows for more flexible SFR changes between time bins — there is evidence for a recent rejuvenation event which briefly boosted the galaxy SFR, followed by rapid quenching. This scenario, then, could explain the observed emission lines: the rejuvenation event initially shifted the line ratios towards the star formation region in the BPT and WHaN diagrams, followed by a shift in the opposite direction as a consequence of the recent quenching. The final line ratios are thus found in the composite region. Interestingly, this may also explain the unusually low $[\text{OIII}]/H\beta$ and $[\text{OIII}]/[\text{OII}]$ line ratios observed in COSMOS-7549: the high-ionization $[\text{OIII}]$ line is expected to disappear after a few Myr since it requires very young and hot stars, while the lower ionization lines such as $H\beta$ and $[\text{OII}]$ can be produced by B-type stars up to ~ 100 Myr after the starburst event ([Quai et al. 2018](#)). Therefore, in this scenario the small amount of ionized gas would come from an extremely recent and abrupt quenching of a minor rejuvenation event.

6. IONIZED GAS OUTFLOWS

The fitting model employed in Section 3, made up of single-Gaussian profiles for each emission line, was not able to successfully fit the spectra of 4 galaxies in the quiescent sample: specifically, galaxies 8013, 11142, 18688, and 19572, all AGN hosts (Table 3). As visible in Figure 4, this simple model is inadequate for an accurate representation of the data, suggesting that more complex physical processes are involved in producing the observed emission. The detailed study of one of the galaxies, COSMOS-11142, has revealed the presence of a powerful outflow, which is responsible for

deviation from the simple Gaussian profile in the ionized gas emission lines ([Belli et al. 2023](#)). We thus employ a multiple-Gaussian model for these four galaxies, in order to investigate the presence of possible ionized gas outflows.

6.1. Emission line broad components

Recent works on rest-frame optical emission of outflowing gas in active galaxies ([Brusa et al. 2015](#); [Übler et al. 2023](#)) employ a fitting model with three Gaussian components for each line: one systemic, narrow component tracing the narrow line region (NLR) and/or star-formation; one very broad, systemic component for permitted transitions, tracing the broad line region (BLR); and finally a third component free to vary in both line width and centroid position, tracing ionized outflows. This model is physically motivated, but suffers from a degeneracy between the two types of broad component. In principle, the degeneracy can be broken by comparing the profiles of different emission lines, since the BLR component is present only in permitted transitions, while the outflow can be traced by both permitted and forbidden transitions. Among the emission lines detected in our sample, the only permitted transitions are $H\beta$, $H\alpha$, and He I. However, $H\beta$ and He I are generally too faint for an accurate modeling of the line profile; moreover, He I shows unique kinematics due to resonant absorption (explored in §6.3). Finally, $H\alpha$ is partially blended with the $[\text{NII}]$ doublet, which makes it impossible to tell the difference between a broadening due to the BLR component of $H\alpha$ or a broadening due to an outflow component underlying all three lines. Therefore, in absence of evident BLR emission (such as for COSMOS-18977, as discussed in § 5), we cannot break this degeneracy for the galaxies in our sample. Since in some cases we clearly observe broad components in forbidden lines, we conclude that ionized outflows must be present, and we adopt a simpler fitting model made up of only two Gaussian components, as done in [Förster Schreiber et al. \(2019\)](#); [Zakamska et al. \(2016\)](#) and [Davies et al. \(2020\)](#). We fix a narrow component at the galaxy redshift with a velocity dispersion $\sigma \leq 300$ km/s; and then we add a broad component with $\sigma \geq 200$ km/s tracing outflows/BLR emission, free to vary with respect to the galaxy systemic velocity. We fit the narrow line profile under each line in Table 2 and fix the same velocity dispersion and redshift for all lines. The broad component is considered only for lines with generally higher signal-to-noise ratios, namely $H\alpha$, $H\beta$, $[\text{OII}]$, $[\text{OIII}]$ and $[\text{NII}]$ doublets. Given the relatively low spectral resolution of our data and the low SNR of the emission lines, we assume that, for a given galaxy, the broad component has

the same velocity dispersion and velocity shift in all the emission lines.

We performed the MCMC fits in the same way as done for the single-Gaussian model (see § 3). The broad component velocity shift is initialized with a flat prior between -1000 and 1000 km/s; the limits on the velocity dispersion prior are 10–300 km/s for the narrow component and 200–2000 km/s for the broad component. The MCMC walkers for the narrow component are initialised in small regions around the best-fit values given from the previous, single-Gaussian fit, while generic starting-point values are given for the broad component walkers.

The results of the double-Gaussian model are compared with the single-Gaussian fit in Figure 13. For each of the four galaxies, we show the single-Gaussian fit in the first panel and the double-Gaussian fit in the second panel, for just one example line. In all cases there is a blueshifted excess that requires a double-Gaussian model, and that we interpret as an outflow of ionized gas leaving the galaxy. The SFR we measure (see §5) is too low to explain the presence of star-formation driven outflows. We can also rule out a star-formation driven fossil outflow: in all galaxies we measure winds velocities (estimated using the velocity offset v and the dispersion σ from the broad fitted component and computing $v_{out} = |v| + 2\sigma$) of $\sim 800 - 1000$ km/s, substantially higher than what is observed in the most powerful star-formation driven outflows at $z \sim 2$ (Davies et al. 2019). The high velocity, together with the lack of any tidal features visible in the near-IR imaging data, also rules out the possibility of tidally-ejected gas after a major merger. The only reasonable origin for the observed outflows is AGN feedback, consistent with the position of these four galaxies on the line diagnostic diagrams.

6.2. Multiphase outflows in quiescent AGN hosts

Many galaxies in the Blue Jay sample host neutral outflows, as shown by an analysis of the Na D absorption line conducted by Davies et al. (2024). In the third panel of Figure 13 we show, for each galaxy with detected ionized outflows, the observed spectrum around the Na D₁, D₂ doublet, together with the stellar absorption as estimated by *Prospector* (red), and the model including excess absorption due to neutral gas (black) as fitted by Davies et al. (2024). Significant blueshifted Na D absorption, indicative of neutral outflows, is present in three of the four systems (IDs 8013, 11142, 18668). In the fourth galaxy with a ionized outflow, COSMOS-19572, Davies et al. (2024) detect *redshifted* Na excess absorption, which is a signature of infalling neutral gas: this fact, combined with the evidence of a nearby companion in NIRC*am* imaging (last

panel of Figure 13) suggests that this is an interacting system. We note, however, that although the NaD absorption in COSMOS-19572 is formally classified as infalling by Davies et al. (2024), its absolute velocity offset is comparable to the measurement error, and therefore this absorption could plausibly be systemic. The interpretation of these observations is not straightforward: most probably, we are looking at an interacting system with a main AGN-hosting galaxy accreting neutral gas from a nearby satellite - which could be fueling the AGN activity - intercepted along the stellar continuum on the 2D spectrum.

The combination of ionized and neutral gas outflows in a subset of quiescent galaxies provides observational evidence for negative AGN feedback on the star formation activity, since we are seeing gas leaving these already gas-poor, quiescent systems. Thus, we can link the observation of ionized gas outflows observed in this sample of quiescent galaxies to the quenching of star-formation in these systems at Cosmic Noon.

There are additional quiescent galaxies in which Davies et al. (2024) observe blueshifted Na D absorption. The only one among these to be classified as an AGN by the line diagnostic diagrams is COSMOS-18688, in which we do not detect any significant ionized gas outflows. We tried fitting a two-component Gaussian profile to its emission lines, but this did not significantly improve the fit with respect to the single-component model. Neutral outflows are detected even in galaxies that are not robustly classified as AGN according to their emission lines. A particularly interesting case is that of galaxy COSMOS-10565 (Figure 14), which has weak emission lines, with the only detected ones being H α and [NII]. This system exhibits the highest [NII]/H α ratio of the whole sample and is the only galaxy classified as “retired” by the WHa*N* diagram (Figure 9). The H α and [NII] line profiles are very blended and closely resemble the profiles observed in COSMOS-11142 (which is characterized by powerful outflows), but their SNR is too low for a meaningful fit with the double-Gaussian profile. If indeed an ionized outflow is present, the outflowing gas is too faint to be seen robustly in the emission lines. The presence of a neutral outflow indicates that this galaxy is probably hosting a low-luminosity AGN, which is undetected due to the weak emission lines. Its low SFR of $\sim 0.1 M_{\odot}/\text{yr}$ and the fact that it is isolated (Figure 4) rule out a major role for star formation feedback and galaxy interactions. This suggests that COSMOS-10565 is not a retired galaxy, despite its location in the WHa*N* diagram, and is consistent with the expectation that the local criterion from Cid Fer-

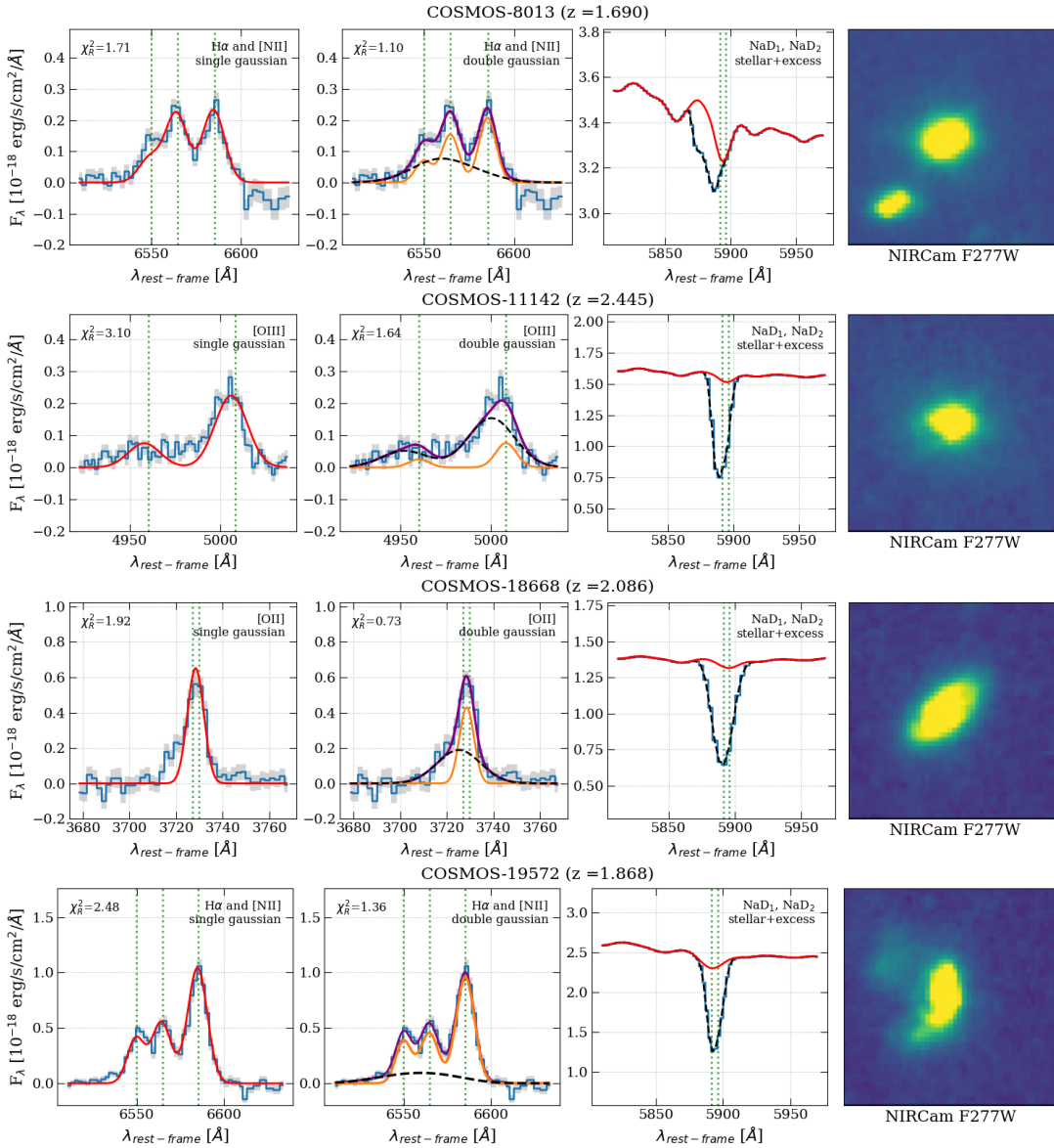


Figure 13. Multiphase outflows in four galaxies of the sample. For each galaxy, the first two panels show the continuum-subtracted spectrum plotted in blue around an example emission line, with a comparison of the single-Gaussian best fit (first panel, red line) to the double-Gaussian best fit (second panel: in purple the total fit, in orange the narrow systemic component and in black dashed the broad shifted component); the third panel shows the neutral gas absorption excess in the Na D line with the best-fit model by [Davies et al. \(2024\)](#), and the fourth panel shows the 3"×3" JWST/NIRCam F277W.

[nandes et al. \(2011\)](#) ($EW_{H\alpha} < 3 \text{ \AA}$) should be lowered at high redshift, as discussed in §4.2.

6.3. The He I line

We report the detection of the high-ionization He I $\lambda 10831 \text{ \AA}$ line in 7 galaxies of the quiescent sample, shown in Figure 15 (we exclude a formal detection in COSMOS-10592 on account of the problems with the data, see § 4). This emission line is detected almost exclusively in galaxies classified as AGN in the BPT — the only exception being COSMOS-10565, which is also likely to host an AGN since it has a neutral outflow (as

discussed above) and COSMOS-11494, in which the line is marginally above detection and the fit does not seem reliable.

In galaxy COSMOS-11142, which presents a wealth of ionized gas emission lines, the He I line is the only one to be redshifted, as shown in [Belli et al. \(2023\)](#). Here we report two more cases – COSMOS-8013 and COSMOS-18668 – where we detected a red excess in the He I emission line. As explained in [Belli et al. \(2023\)](#), this behaviour is likely a consequence of *resonant scattering*, similar to that found in $\text{Ly}\alpha$ emission. This means that we are observing the redshifted (i.e. receding) part

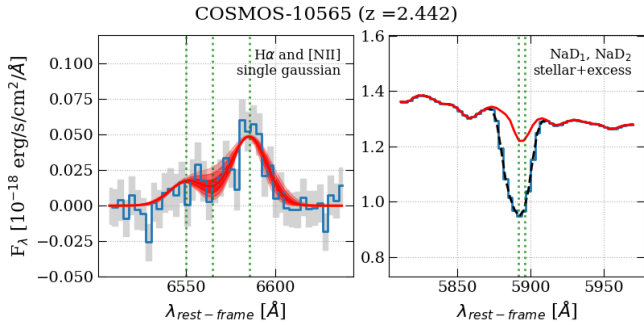


Figure 14. COSMOS-10565 is the only system in the sample to be classified as a retired galaxy by the WHaN diagram. Left: [NII] & H α emission line fits; right: Na D absorption line with best fit from Davies et al. (2024). Despite the WHaN classification, the presence of a neutral outflow suggests that this galaxy hosts an AGN.

of the ionized outflows instead of the approaching one, due to the fact that the He I $\lambda 10831$ transition is metastable and thus photons emitted in the outflows are re-absorbed unless they are redshifted. This constitutes an independent confirmation of the presence of ionized outflows in our sample of quiescent galaxies. Whether it is redshifted or not, the He I emission line in quiescent galaxies may represent a novel, promising indicator to investigate the presence of AGN activity at $z \sim 2$.

7. SUMMARY AND DISCUSSION

In this paper we analyzed the optical rest-frame emission lines of 16 quiescent galaxies observed as part of the Blue Jay survey, a medium-sized Cycle 1 JWST program that targeted 147 galaxies at redshift $1.7 < z < 3.5$ in the COSMOS field. The Blue Jay survey was executed with NIRSpec in MOS mode and obtained spectra between $1 - 5 \mu\text{m}$, covering the $\sim 3000 - 16000 \text{ \AA}$ rest-frame. The present work is the first statistical look at rest-frame optical ionized gas emission lines in a sample of massive quiescent galaxies at $z \sim 2$ with deep spectra from JWST. Quiescent galaxies were selected from the main sample by requiring their SFR, determined by spectro-photometric fitting, to be 1 dex below the main sequence. SFR upper limits determined by the H α line luminosity confirm that the sample is truly quiescent. Nonetheless, we detect emission lines from ionized gas in 12 out of 16 galaxies, representing 75% of the sample. This shows that very deep spectroscopy is able to reveal the presence of ionized gas in the majority of high-redshift quiescent galaxies, confirming a trend established by increasingly deep ground-based observations such as the Heavy Metal survey (Kriek et al. 2023), which detected H α emission in 55% of their quiescent galaxy sample at $z > 1.4$, and small samples of strongly lensed galaxies (e.g., Newman et al. 2018).

7.1. AGN activity in quiescent galaxies at $z \sim 2$

We highlight the detection of multiple emission lines in addition to H α throughout the sample: the exquisite sensitivity of JWST/NIRSpec observations in the near-IR has enabled the detection of weak ionized gas emission lines that would have been otherwise missed by ground-based observations. This, in turn, made it possible to classify galaxies using line ratio diagnostic diagrams, which revealed rampant AGN activity in our sample of massive quiescent galaxies. We find that 8 out of 16 galaxies show emission line ratios compatible with the presence of an active nucleus (50% of the sample). We consider the possibility of contamination of the observed line ratios by fast shocks, but we find no possible sources of shocked gas other than AGN activity itself to be present in these galaxies, apart from the case of the merging system COSMOS-19572. Interestingly, no X-ray detection is found for any of the AGN in our sample, while only one system (COSMOS-18688) is detected in the radio. The main result of this work thus consists in the discovery of a population of never-before-detected AGN at $z \sim 2$ in a sample of apparently inactive massive quiescent galaxies.

To investigate the AGN properties, we start by estimating the bolometric luminosity of each AGN from the observed [OIII] line (Heckman et al. 2004). Most of the AGN exhibit bolometric luminosities of the order of $\sim 10^{44} \text{ erg/s}$; the largest value is found for COSMOS-18688 ($L_{\text{BOL}} = (1.35 \pm 0.02) \cdot 10^{45} \text{ erg/s}$). We then derive the inferred X-ray luminosities in the 2-10 keV range from scaling relations (Duras et al. 2020). We find that most of the sample falls under the flux limits of both the Chandra-COSMOS Legacy Survey Point Source Catalog (Civano et al. 2016) and the COSMOS XMM Point-like Source Catalog (Cappelluti et al. 2009), with the only exceptions being galaxies 19572 and 18688. In any case, the observed [OIII] line luminosity may come also from shock excitation (especially relevant in the case of the merger COSMOS-19572), thus both the bolometric luminosity and inferred X-ray luminosity have to be considered upper limits. We thus conclude that the lack of X-ray detections is expected, given the weak AGN luminosities.

We also estimate the Eddington luminosity L_{Edd} from the black hole mass, which we infer from the $M_{\text{BH}} - \sigma$ relation of McConnell et al. (2011):

$$\left(\frac{M_{\text{BH}}}{10^8 M_{\odot}} \right) = 1.95 \left(\frac{\sigma}{200 \text{ km s}^{-1}} \right)^{5.12}, \quad (1)$$

adopting the stellar velocity dispersions measured from the spectral fits. We show the bolometric luminosity versus the Eddington luminosity for the AGN hosts in

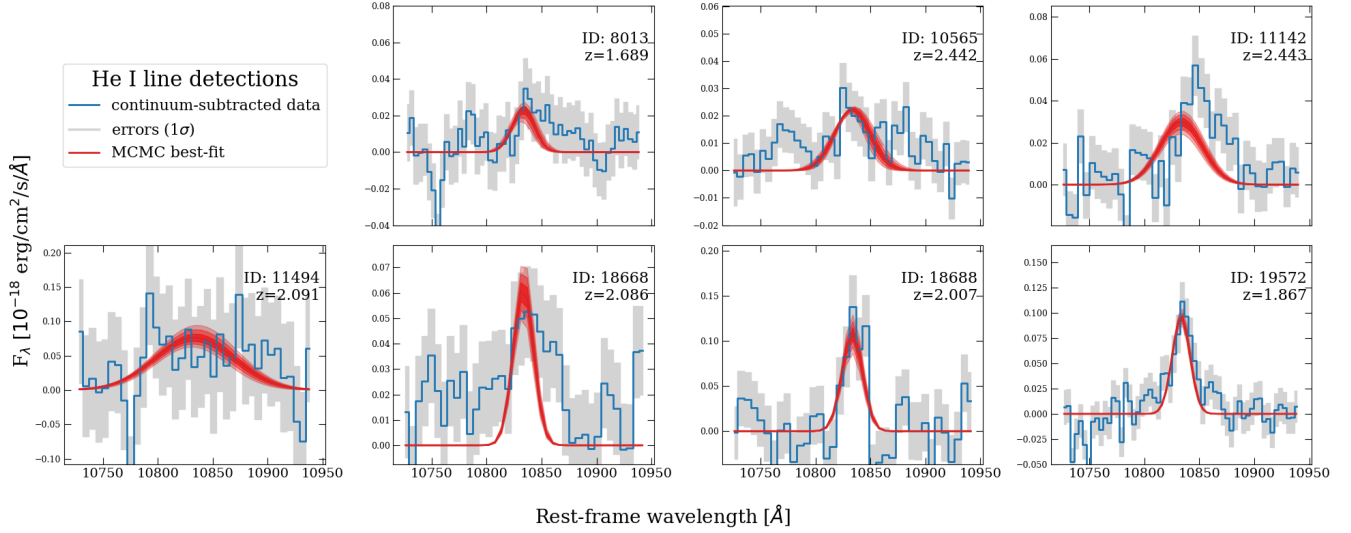


Figure 15. Detected He I $\lambda 10831$ emission lines in the quiescent sample, with single-profile Gaussian fits (in red). Green dashed vertical lines indicate the galactic rest-frame line position. Three galaxies (8013, 11142 and 18668) shows evidence for excess flux in the red side, suggesting the presence of resonant scattering from the receding side of the outflow.

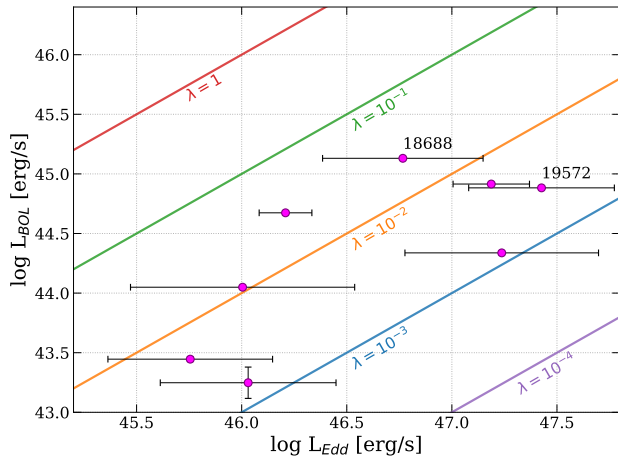


Figure 16. Bolometric luminosity (derived from the observed [OIII] emission line) versus Eddington luminosity (inferred from the stellar velocity dispersion) for the AGN hosts in the sample. Diagonal lines have constant values of Eddington ratio λ .

our sample in Figure 16, where the diagonal lines have constant Eddington ratio L_{bol}/L_{Edd} . Most of the AGN are probably low-luminosity AGN (LL-AGN), with Eddington ratios of $\sim 10^{-3} - 10^{-2}$, typical of a central engine fueled by a Radiatively Inefficient Accretion Flow (RIAF) (see Ho 2008 for a schematic view of the central engine of LL-AGN). As already mentioned in § 4.3, the measured velocity dispersions may be underestimated, thus Eddington ratios may actually be lower than computed here. Even though the high incidence of AGN discovered in this sample of apparently inactive quiescent galaxies has not been seen before at $z \sim 2$, this result is

consistent with what is observed in the local Universe: Ho (2008) analyzed optical emission lines in several surveys of nearby galactic nuclei, finding that 43% of all galaxies show evidence of weak nuclear activity from an accreting SMBH and that the AGN fraction is even more remarkable for galaxies with an obvious bulge component, rising to $\sim 50\% - 70\%$ for Hubble types E-Sb. Our measured AGN incidence of 50%, then, is in line with what is observed at $z \sim 0$, notwithstanding that galaxies with missing line detections could also be hosting LL-AGN out of the sensitivity reach for this survey. Within this framework, it is reasonable to think that many of the Blue Jay galaxies in the star-forming sample may also be hosting a low-luminosity active nucleus whose line emission is however outshined by the nebular emission from HII regions, a problem that does not affect the quiescent sample. To illustrate this idea more clearly, we can follow the relative contributions of star-formation and LL-AGN as a sequence across the WHaN diagram of Figure 17, where symbols have been colored by stellar mass. Gas metallicity also affects line ratios in galaxies of similar masses. In the top left corner (highest $H\alpha$ EWs and lowest [NII]/ $H\alpha$ ratio) we find low-mass, low-metallicity SF galaxies, which probably do not host any AGN: at these low stellar masses, line ratios are determined by star-formation processes and the spread in [NII]/ $H\alpha$ ratio values is likely due to different gas metallicity. Moving towards lower $H\alpha$ EWs, we find higher-mass galaxies: as the specific SFR decreases in the vertical direction, the contribution of a possible LL-AGN in the central regions raises the [NII]/ $H\alpha$ ratio with respect to star-formation only emission, until the massive

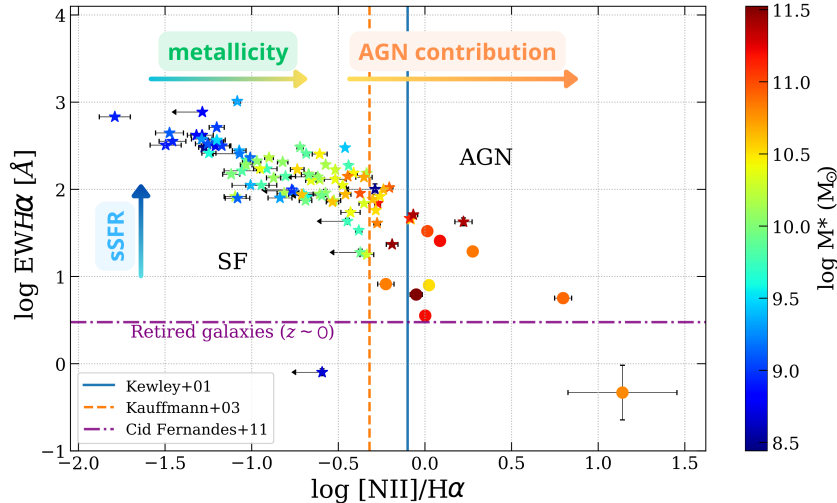


Figure 17. WHaN diagram (see § 4.2), with symbols color-coded by stellar mass. The qualitative trends with specific SFR, metallicity and contribution from AGN are indicated by the arrows. Galaxies in the Blue Jay sample appear to form a diagonal sequence: starting from the low-mass star forming population at the top left corner, as galaxies grow in mass and turn into quiescent galaxies, their specific SFR decreases and the contribution by LL-AGN to the line ratios increases.

quiescent galaxies in the bottom right corner of the diagram are reached, for which the LL-AGN contribution is dominant. For high mass galaxies, metallicity should have a smaller impact on the line ratios, as shown by the relatively small difference in $[\text{NII}]/\text{H}\alpha$ ratio for galaxies of different masses at fixed $\text{H}\alpha$ EW. The observed sequence could thus be seen as an evolutionary track on the WHaN diagram, tracing the evolution of massive galaxies from star-forming to quiescent as driven by the effect of AGN feedback.

7.2. Star-formation quenching by multiphase AGN outflows

We find ionized outflows in a subset of four out of 16 quiescent galaxies, and measure outflow velocities of the order of ~ 1000 km/s. All four galaxies are AGN hosts (according to the line diagnostic diagrams) and display evidence of neutral gas outflows/inflows as well (Davies et al. 2024). Additionally, two other galaxies categorized as AGN hosts exhibit solely neutral phase outflows (COSMOS-10565 and COSMOS-18688). With the exception of COSMOS-19572, for which tidal disruption due to the ongoing merger needs to be considered, the observed outflows can only be driven by AGN activity.

One of the galaxies in our sample is COSMOS-11142, which was studied in detail in Belli et al. (2023). The mass outflow rate in this system is sufficiently large to fully explain the rapid shut-off of star formation, providing one of the first direct observational links between quenching and AGN ejective feedback. However, in this galaxy most of the gas that is being ejected is in the neutral phase, with the ionized phase playing a minor

role. The other galaxies in our sample have ionized outflows that are comparable to, or smaller than, the one observed in COSMOS-11142. Thus, we do not expect that these quiescent galaxies have been quenched solely by the observed ionized outflows. However, many galaxies in our sample do show evidence of neutral outflows, and are therefore similar in many respects to COSMOS-11142, even though none of them is close in terms of providing such a clear quenching picture. One possibility is that COSMOS-11142 was caught at the ideal time, just in the middle of the short-lived, powerful multiphase outflow episode that is responsible for rapidly quenching most of the star formation activity in the galaxy. In this scenario, the other galaxies in our sample are observed in later evolutionary stages: nonetheless, we find that the majority of them still host detectable AGN activity. Thus, our results represent a new, crucial piece of the quenching puzzle, and justifies extrapolating the physical processes observed in one galaxy to the majority of the quiescent population.

Finally, it is possible that the observed LL-AGN activity plays a key role in maintaining quiescence in massive galaxies as they evolve to $z \sim 0$. In the local universe, a particular class of quiescent galaxies exhibiting LL-AGN activity and ionized gas winds, called “red geysers”, has already been observed (Cheung et al. 2016; Roy et al. 2018, 2021). Local LL-AGN are associated to RIAFs (Ho 2008), which have a tendency to drive powerful winds (Narayan & Yi 1995; Blandford & Begelman 1999) whose thermal and kinetic energy is deposited in the surrounding ISM. Almeida et al. (2023) developed a model for LL-AGN feedback through galaxy-scale winds pro-

duced by RIAFs and showed that these winds, especially if long-lived (on timescales of 10 Myr or longer) can prevent gas collapse and effectively quench star-formation in massive galaxies. There could be then a direct link between the LL-AGN activity at Cosmic Noon, which is responsible for rapid quenching, and the maintenance mode observed in local "red geysers".

Facilities: JWST(NIRSpec)

Software: EMCEE Python library (Foreman-Mackey et al. 2013), Prospector (Johnson et al. 2021), EAZY (Brammer et al. 2008)

1 We thank Salvatore Quai, Ivan Lopez, Raffaele Pascale,
 2 Marcella Brusa and Elena Bertola for the help and for
 3 the illuminating discussions.
 4 The Blue Jay Survey is funded in part by STScI
 5 Grant JWST-GO-01810. SB is supported by the the
 6 ERC Starting Grant "Red Cardinal", GA 101076080.
 7 RD is supported by the Australian Research Council
 8 Centre of Excellence for All Sky Astrophysics in
 9 3 Dimensions (ASTRO 3D), through project number
 10 CE170100013. RE acknowledges the support from grant
 11 numbers 21-atp21-0077, NSF AST-1816420, and HST-
 12 GO-16173.001-A as well as the Institute for Theory and
 13 Computation at the Center for Astrophysics. RW ac-
 14 knowledges funding of a Leibniz Junior Research Group
 15 (project number J131/2022). This work is based on
 16 observations made with the NASA/ESA/CSA James
 17 Webb Space Telescope. The data were obtained from
 18 the Mikulski Archive for Space Telescopes at the Space
 19 Telescope Science Institute, which is operated by the
 20 Association of Universities for Research in Astronomy,
 21 Inc., under NASA contract NAS 5-03127 for JWST.
 22 These observations are associated with program GO
 23 1810. This work also makes use of observations taken by
 24 the 3D-HST Treasury Program (GO 12177 and 12328)
 25 with the NASA/ESA HST, which is operated by the
 26 Association of Universities for Research in Astronomy,
 27 Inc., under NASA contract NAS5-26555.

APPENDIX

A. FULL SPECTRAL MEASUREMENTS

In Table 4 we display the full set of spectral measurements for each galaxy in the sample.

REFERENCES

- Almeida, I., Nemmen, R., & Riffel, R. A. 2023, MNRAS, 526, 217, doi: [10.1093/mnras/stad2673](https://doi.org/10.1093/mnras/stad2673)
- Baldwin, J. A., Phillips, M. M., & Terlevich, R. 1981, PASP, 93, 5, doi: [10.1086/130766](https://doi.org/10.1086/130766)
- Belfiore, F., Maiolino, R., Maraston, C., et al. 2016, MNRAS, 461, 3111, doi: [10.1093/mnras/stw1234](https://doi.org/10.1093/mnras/stw1234)
- Belli, S., Newman, A. B., & Ellis, R. S. 2019, ApJ, 874, 17, doi: [10.3847/1538-4357/ab07af](https://doi.org/10.3847/1538-4357/ab07af)
- Belli, S., Genzel, R., Förster Schreiber, N. M., et al. 2017, ApJL, 841, L6, doi: [10.3847/2041-8213/aa70e5](https://doi.org/10.3847/2041-8213/aa70e5)
- Belli, S., Park, M., Davies, R. L., et al. 2023, arXiv e-prints, arXiv:2308.05795, doi: [10.48550/arXiv.2308.05795](https://doi.org/10.48550/arXiv.2308.05795)

Table 4. Spectral fitting results

COSMOS ID	z_{gas}	σ_{gas} (km s^{-1})	Flux ($10^{-18} \text{ erg s}^{-1} \text{ cm}^{-2}$)									
			[OII] (4)	[NeIII] (5)	H β (6)	[OIII]5007 (7)	H α (8)	[NII]6583 (9)	[SII]6716 (10)	[SII]6731 (11)	He I (12)	
7549	2.6238	$157.07^{+10.40}_{-10.20}$	$2.63^{+0.28}_{-0.26}$	< 0.020	$0.76^{+0.06}_{-0.06}$	< 0.022	$2.14^{+0.13}_{-0.13}$	$1.27^{+0.12}_{-0.11}$	$0.68^{+0.11}_{-0.11}$	< 0.651	< 0.201	
8013	1.6894	$261.08^{+4.38}_{-3.94}$	$8.65^{+0.60}_{-0.59}$	$1.06^{+0.14}_{-0.14}$	< 0.987	$4.51^{+0.13}_{-0.12}$	$9.13^{+0.13}_{-0.13}$	$9.63^{+0.14}_{-0.13}$	$3.29^{+0.31}_{-0.29}$	$2.02^{+0.32}_{-0.30}$	$1.59^{+0.17}_{-0.16}$	
8469	< 0.126	< 0.212	< 0.643	< 3.75	< 0.142	< 0.098	< 0.129	< 0.100	< 0.201	
9395	2.1268	$400.47^{+27.69}_{-26.93}$	$2.44^{+0.35}_{-0.34}$	< 0.026	< 0.166	< 1.055	< 0.604	< 0.747	< 0.039	< 0.020	< 0.935	
10128	1.8517	$235.24^{+8.01}_{-7.46}$	$0.55^{+0.03}_{-0.03}$	< 0.002	...	$0.95^{+0.04}_{-0.04}$	$2.91^{+0.11}_{-0.11}$	$2.93^{+0.11}_{-0.11}$	< 1.649	< 0.873	< 0.261	
10339	2.3636	$536.04^{+59.23}_{-54.90}$	$1.54^{+0.34}_{-0.33}$...	$0.30^{+0.10}_{-0.09}$	< 0.160	
10400	< 0.274	< 0.728	< 0.048	< 0.51	< 0.078	< 0.116	< 0.093	
10565	2.4416	$425.70^{+31.50}_{-30.41}$	$110.10^{+55.80}_{-53.27}$	$49.51^{+34.44}_{-33.30}$	< 0.028	< 0.371	$0.29^{+0.25}_{-0.20}$	$4.07^{+0.26}_{-0.27}$	< 1.054	< 0.155	$3.12^{+0.28}_{-0.27}$	
10592	< 0.001	< 0.27	< 0.006	< 0.007	< 0.017	< 0.008	< 8.88	
11142	2.4434	$522.15^{+9.26}_{-9.05}$	$6.58^{+0.25}_{-0.24}$	$2.13^{+0.19}_{-0.19}$	< 0.049	$17.18^{+0.31}_{-0.31}$	$5.65^{+0.62}_{-0.63}$	$35.42^{+0.63}_{-0.63}$	$2.39^{+0.52}_{-0.51}$	$4.53^{+0.51}_{-0.51}$	$5.06^{+0.38}_{-0.39}$	
11494	2.0909	$985.43^{+10.85}_{-23.10}$	$7.59^{+1.94}_{-1.77}$	< 0.167	< 0.123	< 0.060	$24.57^{+2.76}_{-3.37}$	$2.68^{+2.68}_{-1.91}$	< 0.702	< 0.512	$21.30^{+1.78}_{-1.89}$	
16419	1.9257	$437.70^{+10.30}_{-10.40}$	$43.11^{+5.56}_{-5.53}$	< 0.622	< 5.293	$14.97^{+0.63}_{-0.62}$	$28.12^{+1.61}_{-1.58}$	$25.03^{+1.46}_{-1.45}$	$28.32^{+1.87}_{-1.82}$	$18.04^{+1.82}_{-1.86}$	< 1.610	
18668	2.0857	$204.44^{+3.68}_{-3.43}$	$17.66^{+1.15}_{-1.18}$	< 0.206	$3.74^{+0.21}_{-0.21}$	$5.99^{+0.21}_{-0.21}$	$29.28^{+0.44}_{-0.45}$	$30.23^{+0.42}_{-0.41}$	$6.84^{+0.35}_{-0.35}$	$4.35^{+0.34}_{-0.34}$	$4.44^{+0.33}_{-0.32}$	
18688	2.0068	$205.46^{+2.31}_{-2.30}$	$16.01^{+0.46}_{-0.44}$	$4.19^{+0.36}_{-0.36}$	$9.06^{+0.33}_{-0.32}$	$39.87^{+0.44}_{-0.44}$	$48.60^{+0.74}_{-0.72}$	$59.37^{+0.74}_{-0.71}$	$7.48^{+0.62}_{-0.61}$	$7.60^{+0.61}_{-0.61}$	$7.57^{+0.56}_{-0.55}$	
19572	1.8674	$201.19^{+2.06}_{-1.99}$	$9.98^{+1.05}_{-1.05}$	< 2.360	$3.07^{+0.17}_{-0.18}$	$25.62^{+0.22}_{-0.22}$	$22.34^{+0.31}_{-0.33}$	$42.17^{+0.31}_{-0.31}$	$5.45^{+0.33}_{-0.34}$	$4.23^{+0.31}_{-0.31}$	$5.56^{+0.19}_{-0.19}$	
21477	< 4.690	< 1.225	< 0.147	< 0.939	< 0.450	< 0.842	< 0.028	< 0.995	< 0.358	

NOTE—Flux measurement for fitted emission lines in the quiescent sample.

- Bertola, F., Buson, L. M., & Zeilinger, W. W. 1992, *ApJ*, 401, L79, doi: [10.1086/186675](https://doi.org/10.1086/186675)
- Binette, L., Magris, C. G., Stasińska, G., & Bruzual, A. G. 1994, *A & A*, 292, 13
- Blandford, R. D., & Begelman, M. C. 1999, *MNRAS*, 303, L1, doi: [10.1046/j.1365-8711.1999.02358.x](https://doi.org/10.1046/j.1365-8711.1999.02358.x)
- Brammer, G. B., van Dokkum, P. G., & Coppi, P. 2008, *ApJ*, 686, 1503, doi: [10.1086/591786](https://doi.org/10.1086/591786)
- Brammer, G. B., van Dokkum, P. G., Franx, M., et al. 2012, *ApJS*, 200, 13, doi: [10.1088/0067-0049/200/2/13](https://doi.org/10.1088/0067-0049/200/2/13)
- Brusa, M., Bongiorno, A., Cresci, G., et al. 2015, *mnras*, 446, 2394, doi: [10.1093/mnras/stu2117](https://doi.org/10.1093/mnras/stu2117)
- Buson, L. M., Sadler, E. M., Zeilinger, W. W., et al. 1993, *A & A*, 280, 409
- Byler, N., Dalcanton, J. J., Conroy, C., et al. 2019, *AJ*, 158, 2, doi: [10.3847/1538-3881/ab1b70](https://doi.org/10.3847/1538-3881/ab1b70)
- Calzetti, D., Armus, L., Bohlin, R. C., et al. 2000, *ApJ*, 533, 682, doi: [10.1086/308692](https://doi.org/10.1086/308692)
- Cappelluti, N., Brusa, M., Hasinger, G., et al. 2009, *A & A*, 497, 635, doi: [10.1051/0004-6361/200810794](https://doi.org/10.1051/0004-6361/200810794)
- Carnall, A. C., McLure, R. J., Dunlop, J. S., et al. 2023, *Nature*, 619, 716, doi: [10.1038/s41586-023-06158-6](https://doi.org/10.1038/s41586-023-06158-6)
- Charlot, S., & Fall, S. M. 2000, *ApJ*, 539, 718, doi: [10.1086/309250](https://doi.org/10.1086/309250)
- Cheung, E., Bundy, K., Cappellari, M., et al. 2016, *Nature*, 533, 504, doi: [10.1038/nature18006](https://doi.org/10.1038/nature18006)
- Cid Fernandes, R., Stasińska, G., Mateus, A., & Vale Asari, N. 2011, *MNRAS*, 413, 1687, doi: [10.1111/j.1365-2966.2011.18244.x](https://doi.org/10.1111/j.1365-2966.2011.18244.x)
- Cid Fernandes, R., Stasińska, G., Schlickmann, M. S., et al. 2010, *MNRAS*, 403, 1036, doi: [10.1111/j.1365-2966.2009.16185.x](https://doi.org/10.1111/j.1365-2966.2009.16185.x)
- Civano, F., Marchesi, S., Comastri, A., et al. 2016, *ApJ*, 819, 62, doi: [10.3847/0004-637X/819/1/62](https://doi.org/10.3847/0004-637X/819/1/62)
- Conroy, C., Gunn, J. E., & White, M. 2009, *ApJ*, 699, 486, doi: [10.1088/0004-637X/699/1/486](https://doi.org/10.1088/0004-637X/699/1/486)
- Davies, R. L., Förster Schreiber, N. M., Übler, H., et al. 2019, *ApJ*, 873, 122, doi: [10.3847/1538-4357/ab06f1](https://doi.org/10.3847/1538-4357/ab06f1)
- Davies, R. L., Förster Schreiber, N. M., Lutz, D., et al. 2020, *ApJ*, 894, 28, doi: [10.3847/1538-4357/ab86ad](https://doi.org/10.3847/1538-4357/ab86ad)
- Davies, R. L., Belli, S., Park, M., et al. 2024, *MNRAS*, 528, 4976, doi: [10.1093/mnras/stae327](https://doi.org/10.1093/mnras/stae327)
- de Graaff, A., Rix, H.-W., Carniani, S., et al. 2024, *A&A*, 684, A87, doi: [10.1051/0004-6361/202347755](https://doi.org/10.1051/0004-6361/202347755)
- D'Eugenio, F., Perez-Gonzalez, P., Maiolino, R., et al. 2023, *arXiv e-prints*, arXiv:2308.06317, doi: [10.48550/arXiv.2308.06317](https://doi.org/10.48550/arXiv.2308.06317)
- Dopita, M. A., Kewley, L. J., Heisler, C. A., & Sutherland, R. S. 2000, *ApJ*, 542, 224, doi: [10.1086/309538](https://doi.org/10.1086/309538)
- Dopita, M. A., & Sutherland, R. S. 1995, *ApJ*, 455, 468, doi: [10.1086/176596](https://doi.org/10.1086/176596)
- Dunlop, J. S., Abraham, R. G., Ashby, M. L. N., et al. 2021, PRIMER: Public Release IMaging for Extragalactic Research, JWST Proposal. Cycle 1, ID. #1837
- Duras, F., Bongiorno, A., Ricci, F., et al. 2020, *A&A*, 636, A73, doi: [10.1051/0004-6361/201936817](https://doi.org/10.1051/0004-6361/201936817)
- Foreman-Mackey, D., Hogg, D. W., Lang, D., & Goodman, J. 2013, *Publications of the Astronomical Society of the Pacific*, 125, 306–312, doi: [10.1086/670067](https://doi.org/10.1086/670067)
- Förster Schreiber, N. M., Übler, H., Davies, R. L., et al. 2019, *ApJ*, 875, 21, doi: [10.3847/1538-4357/ab0ca2](https://doi.org/10.3847/1538-4357/ab0ca2)
- Grogin, N. A., Kocevski, D. D., Faber, S. M., et al. 2011, *ApJS*, 197, 35, doi: [10.1088/0067-0049/197/2/35](https://doi.org/10.1088/0067-0049/197/2/35)
- Heckman, T., Borthakur, S., Wild, V., Schiminovich, D., & Bordoloi, R. 2017, *ApJ*, 846, 151, doi: [10.3847/1538-4357/aa80dc](https://doi.org/10.3847/1538-4357/aa80dc)
- Heckman, T. M., Baum, S. A., van Breugel, W. J. M., & McCarthy, P. 1989, *ApJ*, 338, 48, doi: [10.1086/167181](https://doi.org/10.1086/167181)
- Heckman, T. M., Kauffmann, G., Brinchmann, J., et al. 2004, *ApJ*, 613, 109, doi: [10.1086/422872](https://doi.org/10.1086/422872)
- Ho, I. T., Medling, A. M., Bland-Hawthorn, J., et al. 2016, *MNRAS*, 457, 1257, doi: [10.1093/mnras/stw017](https://doi.org/10.1093/mnras/stw017)
- Ho, L. C. 2008, *ARA&A*, 46, 475, doi: [10.1146/annurev.astro.45.051806.110546](https://doi.org/10.1146/annurev.astro.45.051806.110546)
- Johnson, B. D., Leja, J., Conroy, C., & Speagle, J. S. 2021, *ApJS*, 254, 22, doi: [10.3847/1538-4365/abef67](https://doi.org/10.3847/1538-4365/abef67)
- Kauffmann, G., Heckman, T. M., White, S. D. M., et al. 2003, *MNRAS*, 341, 54, doi: [10.1046/j.1365-8711.2003.06292.x](https://doi.org/10.1046/j.1365-8711.2003.06292.x)
- Kennicutt, Robert C., J. 1998, *ARA & A*, 36, 189, doi: [10.1146/annurev.astro.36.1.189](https://doi.org/10.1146/annurev.astro.36.1.189)
- Kewley, L. J., Dopita, M. A., Sutherland, R. S., Heisler, C. A., & Trevena, J. 2001, *ApJ*, 556, 121, doi: [10.1086/321545](https://doi.org/10.1086/321545)
- Kewley, L. J., Groves, B., Kauffmann, G., & Heckman, T. 2006, *MNRAS*, 372, 961, doi: [10.1111/j.1365-2966.2006.10859.x](https://doi.org/10.1111/j.1365-2966.2006.10859.x)
- Kewley, L. J., Nicholls, D. C., & Sutherland, R. S. 2019, *ARA & A*, 57, 511, doi: [10.1146/annurev-astro-081817-051832](https://doi.org/10.1146/annurev-astro-081817-051832)
- Kim, D.-W. 1989, *ApJ*, 346, 653, doi: [10.1086/168048](https://doi.org/10.1086/168048)
- Koekemoer, A. M., Faber, S. M., Ferguson, H. C., et al. 2011, *ApJS*, 197, 36, doi: [10.1088/0067-0049/197/2/36](https://doi.org/10.1088/0067-0049/197/2/36)
- Kriek, M., & Conroy, C. 2013, *ApJL*, 775, L16, doi: [10.1088/2041-8205/775/1/L16](https://doi.org/10.1088/2041-8205/775/1/L16)
- Kriek, M., Beverage, A. G., Price, S. H., et al. 2023, *arXiv e-prints*, arXiv:2311.16232, doi: [10.48550/arXiv.2311.16232](https://doi.org/10.48550/arXiv.2311.16232)

- Leja, J., Tacchella, S., & Conroy, C. 2019, *ApJL*, 880, L9, doi: [10.3847/2041-8213/ab2f8c](https://doi.org/10.3847/2041-8213/ab2f8c)
- Leja, J., Speagle, J. S., Ting, Y.-S., et al. 2022, *ApJ*, 936, 165, doi: [10.3847/1538-4357/ac887d](https://doi.org/10.3847/1538-4357/ac887d)
- Macchetto, F., Pastoriza, M., Caon, N., et al. 1996, *A & A*, 120, 463
- Madau, P., & Dickinson, M. 2014, *ARAA*, 52, 415, doi: [10.1146/annurev-astro-081811-125615](https://doi.org/10.1146/annurev-astro-081811-125615)
- Man, A. W. S., Zabl, J., Brammer, G. B., et al. 2021, *ApJ*, 919, 20, doi: [10.3847/1538-4357/ac0ae3](https://doi.org/10.3847/1538-4357/ac0ae3)
- McConnell, N. J., Ma, C.-P., Gebhardt, K., et al. 2011, *Nature*, 480, 215, doi: [10.1038/nature10636](https://doi.org/10.1038/nature10636)
- Medling, A. M., U, V., Rich, J. A., et al. 2015, *MNRAS*, 448, 2301, doi: [10.1093/mnras/stv081](https://doi.org/10.1093/mnras/stv081)
- Momcheva, I. G., Brammer, G. B., van Dokkum, P. G., et al. 2016, *ApJS*, 225, 27, doi: [10.3847/0067-0049/225/2/27](https://doi.org/10.3847/0067-0049/225/2/27)
- Muzzin, A., Marchesini, D., Stefanon, M., et al. 2013, *ApJ*, 777, 18, doi: [10.1088/0004-637X/777/1/18](https://doi.org/10.1088/0004-637X/777/1/18)
- Narayan, R., & Yi, I. 1995, *ApJ*, 452, 710, doi: [10.1086/176343](https://doi.org/10.1086/176343)
- Newman, A. B., Belli, S., & Ellis, R. S. 2015, *ApJL*, 813, L7, doi: [10.1088/2041-8205/813/1/L7](https://doi.org/10.1088/2041-8205/813/1/L7)
- Newman, A. B., Belli, S., Ellis, R. S., & Patel, S. G. 2018, *ApJ*, 862, 125, doi: [10.3847/1538-4357/aacd4d](https://doi.org/10.3847/1538-4357/aacd4d)
- Osterbrock, D. E. 1989, *Astrophysics of gaseous nebulae and active galactic nuclei*
- Osterbrock, D. E., & Ferland, G. J. 2006, *Astrophysics of gaseous nebulae and active galactic nuclei*
- Park, M., Belli, S., Conroy, C., et al. 2023, *The Astrophysical Journal*, 953, 119, doi: [10.3847/1538-4357/acd54a](https://doi.org/10.3847/1538-4357/acd54a)
- Park, M., Belli, S., Conroy, C., et al. 2024, *arXiv e-prints*, arXiv:2404.17945, doi: [10.48550/arXiv.2404.17945](https://doi.org/10.48550/arXiv.2404.17945)
- Phillips, M. M., Jenkins, C. R., Dopita, M. A., Sadler, E. M., & Binette, L. 1986, *AJ*, 91, 1062, doi: [10.1086/114083](https://doi.org/10.1086/114083)
- Quai, S., Pozzetti, L., Citro, A., Moresco, M., & Cimatti, A. 2018, *MNRAS*, 478, 3335, doi: [10.1093/mnras/sty1045](https://doi.org/10.1093/mnras/sty1045)
- Rich, J. A., Kewley, L. J., & Dopita, M. A. 2011, *ApJ*, 734, 87, doi: [10.1088/0004-637X/734/2/87](https://doi.org/10.1088/0004-637X/734/2/87)
- . 2014, *ApJL*, 781, L12, doi: [10.1088/2041-8205/781/1/L12](https://doi.org/10.1088/2041-8205/781/1/L12)
- Roy, N., Bundy, K., Cheung, E., et al. 2018, *ApJ*, 869, 117, doi: [10.3847/1538-4357/aaee72](https://doi.org/10.3847/1538-4357/aaee72)
- Roy, N., Bundy, K., Nevin, R., et al. 2021, *ApJ*, 913, 33, doi: [10.3847/1538-4357/abf1e6](https://doi.org/10.3847/1538-4357/abf1e6)
- Sanders, R. L., Shapley, A. E., Reddy, N. A., et al. 2020, *MNRAS*, 491, 1427, doi: [10.1093/mnras/stz3032](https://doi.org/10.1093/mnras/stz3032)
- Schinnerer, E., Carilli, C. L., Scoville, N. Z., et al. 2004, *AJ*, 128, 1974, doi: [10.1086/424860](https://doi.org/10.1086/424860)
- Shields, J. C. 1992, *ApJL*, 399, L27, doi: [10.1086/186598](https://doi.org/10.1086/186598)
- Skelton, R. E., Whitaker, K. E., Momcheva, I. G., et al. 2014, *ApJS*, 214, 24, doi: [10.1088/0067-0049/214/2/24](https://doi.org/10.1088/0067-0049/214/2/24)
- Smolčić, V., Novak, M., Bondi, M., et al. 2017, *A&A*, 602, A1, doi: [10.1051/0004-6361/201628704](https://doi.org/10.1051/0004-6361/201628704)
- Sparks, W. B., Macchetto, F., & Golombek, D. 1989, *ApJ*, 345, 153, doi: [10.1086/167890](https://doi.org/10.1086/167890)
- Stasińska, G., Cid Fernandes, R., Mateus, A., Sodré, L., & Asari, N. V. 2006, *MNRAS*, 371, 972, doi: [10.1111/j.1365-2966.2006.10732.x](https://doi.org/10.1111/j.1365-2966.2006.10732.x)
- Steidel, C. C., Strom, A. L., Pettini, M., et al. 2016, *ApJ*, 826, 159, doi: [10.3847/0004-637X/826/2/159](https://doi.org/10.3847/0004-637X/826/2/159)
- Straatman, C. M. S., Spitler, L. R., Quadri, R. F., et al. 2016, *ApJ*, 830, 51, doi: [10.3847/0004-637X/830/1/51](https://doi.org/10.3847/0004-637X/830/1/51)
- Strom, A. L., Steidel, C. C., Rudie, G. C., et al. 2017, *ApJ*, 836, 164, doi: [10.3847/1538-4357/836/2/164](https://doi.org/10.3847/1538-4357/836/2/164)
- Tacchella, S., Conroy, C., Faber, S. M., et al. 2022, *ApJ*, 926, 134, doi: [10.3847/1538-4357/ac449b](https://doi.org/10.3847/1538-4357/ac449b)
- Toft, S., Zabl, J., Richard, J., et al. 2017, *Nature*, 546, 510, doi: [10.1038/nature22388](https://doi.org/10.1038/nature22388)
- Tremonti, C. A., Heckman, T. M., Kauffmann, G., et al. 2004, *ApJ*, 613, 898, doi: [10.1086/423264](https://doi.org/10.1086/423264)
- Übler, H., Maiolino, R., Curtis-Lake, E., et al. 2023, *arXiv e-prints*, arXiv:2302.06647, doi: [10.48550/arXiv.2302.06647](https://doi.org/10.48550/arXiv.2302.06647)
- Veilleux, S., & Osterbrock, D. E. 1987, *ApJS*, 63, 295, doi: [10.1086/191166](https://doi.org/10.1086/191166)
- Voit, G. M., & Donahue, M. 1990, *ApJL*, 360, L15, doi: [10.1086/185801](https://doi.org/10.1086/185801)
- Whitaker, K. E., Labbé, I., van Dokkum, P. G., et al. 2011, *ApJ*, 735, 86, doi: [10.1088/0004-637X/735/2/86](https://doi.org/10.1088/0004-637X/735/2/86)
- Williams, R. J., Quadri, R. F., Franx, M., van Dokkum, P., & Labbé, I. 2009, *ApJ*, 691, 1879, doi: [10.1088/0004-637X/691/2/1879](https://doi.org/10.1088/0004-637X/691/2/1879)
- Zakamska, N. L., Hamann, F., Pâris, I., et al. 2016, *mnras*, 459, 3144, doi: [10.1093/mnras/stw718](https://doi.org/10.1093/mnras/stw718)